ACS OMEGA

Open Access

http://pubs.acs.org/journal/acsodf

Article

The Mechanism of Ozone Oxidation of Coal and the Revelation of Coal Macromolecular Structure by Oxidation Products

Qing Luo, Wenli Liu,* and Qiming Zhuo*

Cite This: *ACS Omega* 2024, 9, 753−770

Read Online

ACCESS | Metrics & More | Article Recommendations | Supporting Information

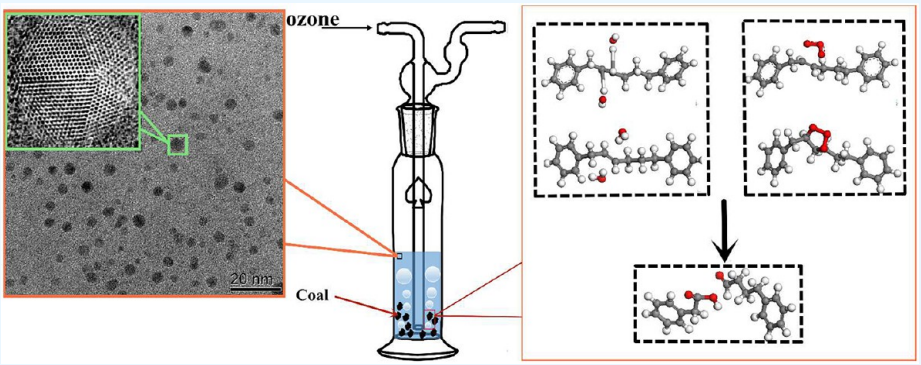

ABSTRACT: Ozone was injected into a coal-water suspension, and an HRTEM test was carried out on the separated oxidation products. The results show that from the perspective of visualization the macromolecular network structure of coal contains a large number of graphite-like structures. However, the chemical reaction mechanism between the coal surface and O_3 is not clear, and the microscopic formation mechanism of oxygen-containing functional groups in carbon quantum dots has not been explained. As a result, the reaction process between O_3 and methylene on the coal surface was studied by the DFT method. We found that OH• generated by O_3 in water can oxidize two adjacent carbon atoms in methylene into double bonds (C═C), and finally, aldehydes and carboxylic acids were generated. By calculation of thermodynamic parameters ΔG and ΔH, it is found that all reactions are spontaneous exothermic processes. The above chemical reaction is based on the physical adsorption of OH• with $Ar-(CH_2)_6-Ar$ and O_3 with $Ar-CH_2-CH=CH-(CH_2)_3-Ar$. The calculated adsorption energies of the two systems are −9.41 and −12.55 kcal/mol, respectively. Then, the charge transfer and atomic orbital interaction before and after adsorption are analyzed from the perspectives of Mulliken charge, density of states, deformation density, and total charge density. The results show that the electrostatic attraction is the main driving force of adsorption. The ether bond (C−O−C) in coal is finally oxidized to an ester group (RCOOR′), the hydroxyl group ($CH_2-CH-OH$) on the aliphatic chain is oxidized to a carbonyl group ($CH_2-C=O$), and the benzene with two OH• forms phenol hydroxyl and one molecule of water. Finally, the coal and the corresponding coal-based carbon quantum dots were investigated by infrared spectroscopy; the difference in functional groups before and after oxidation was clarified, and the result was in good agreement with the simulation.

1. INTRODUCTION

Coal is an important energy resource for social and economic development.[1] Some studies have shown that under the action of strong oxidants, moderate or deep oxidation of coal will occur, and a kind of useful functional material will be separated from the coal surface, namely, coal-based carbon quantum dots.[2] They are composed of one or several layers of carbon sheets, with general lateral dimensions below 10 nm.[3] For example, Xu et al.[4] oxidized anthracite, bituminous coal, and lignite with concentrated sulfuric acid and concentrated nitric acid to prepare corresponding carbon quantum dots and doped them with N, P, and S elements. They found that the optical properties of doped carbon quantum dots are highly sensitive to the concentration of Pb^{2+} in water. Dong et al.[5] oxidized six coals of different coalification for 12 h by nitric acid solution at 130 °C, and two kinds of coal-based carbon quantum dots were obtained after centrifugation. The average thickness and size of oxidation products is 0.5 and 10 nm, respectively.

Coal can be oxidized to obtain carbon quantum dots mainly due to its molecular structure. However, because the structure of coal is so complex;[6−8] although, many scholars have performed much research,[9−12] there is still no unified chemical

Received: August 31, 2023
Revised: October 21, 2023
Accepted: November 23, 2023
Published: December 19, 2023

https://doi.org/10.1021/acsomega.3c06525
ACS Omega 2024, 9, 753−770

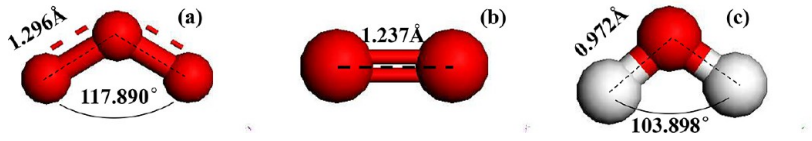

Figure 1. Optimized structure: (a) ozone, (b) oxygen, and (c) water.

formula. At present, the general understanding of coal molecules is that coal is a mixture of compounds with similar structures and different molecular weights, which are connected by methylene and ether bonds to form macromolecular network structures.[13] This is the premise that coal's surface oxidation can obtain carbon quantum dots, and the commonly used oxidants are concentrated sulfuric acid,[14] concentrated nitric acid,[15] hydrogen peroxide,[16] ozone,[17] etc. Because coal-based carbon quantum dots are the oxidation products of molecular fragments stripped from the macromolecular structure of coal, it is of great significance to study the atomic arrangement and bonding forms in carbon quantum dots for analysis of the macromolecular structure of coal.

Among the oxidants mentioned above, concentrated acid is corrosive and will cause serious pollution to the environment, while ozone can decompose into oxygen spontaneously, which is an environmentally friendly oxidant.[17] The reaction between ozone and coal is a moderate oxidation process. Injecting ozone into a coal-water suspension can realize the surface oxidation of coal, and some oxidation products can also be obtained. For carbon quantum dots, many studies have been performed on their size distribution,[18] optical properties,[19] biological cell labeling,[20] metal ion detection,[21] preparation methods,[22−24] and the use of intermediate materials,[25] and they have made significant progress. However, few researchers have explored the formation process of the carbon quantum dot preparation. Although some scholars[26,27] have compared the infrared spectra of coal-based carbon quantum dots with those of coal and found that the oxygen-containing functional groups of the two are quite different, almost no one has studied the surface oxidation mechanism of coal by ozone at the microscopic level. Cai[28] confirmed the change in oxygen-containing functional groups after coal oxidation through experiments, but few studies have directly revealed the formation pathways of phenolic hydroxyl, ester, aldehyde and carboxyl groups in coal-based carbon quantum dots at the atomic level. Therefore, in this study, we employed ozone to oxidize three coals and used a high-resolution transmission electron microscope to study the morphology and lattice fringes of the oxidation products obtained from the coal surface, aiming to reveal the molecular structure of the coal from the perspective of visualization. All reactions were carried out at room temperature and pressure. We also adopted density functional theory and a method to explore the mechanism of coal oxidation by ozone to reveal the formation process of each functional group from the atomic and electronic levels. This study may lay a theoretical foundation for the in-depth utilization of carbon quantum dot functional materials and the study of the macromolecular structure of coal.

2. EXPERIMENTAL AND COMPUTATIONAL METHODS

2.1. Experimental Method. First, float-and-sink experiments of sub-bituminous coal, bituminous coal, and anthracite were carried out to remove minerals; then, the obtained demineralized coal was crushed; and finally, screening experiments were performed. Ten grams of each coal was put into a 500 mL gas washing bottle, and 200 mL of deionized water was added. The coal-water solution was treated under ultrasonic conditions of 40 kHz for 60 min to obtain the coal-water suspension. Then, ozone (74.8 mg/L) was injected into the suspension at a flow rate of 1 L/min to oxidize the coal for 3 h. Next, the samples were transferred to an HC-2062 high-speed centrifuge and separated for 30 min at a speed of 14 000 rpm (centrifugal acceleration is 13148 g) to obtain the supernatant. Finally, the supernatant was moved to a clean beaker; moisture was evaporated in a water bath at 65 °C, and a powder of coal-based carbon quantum dots was obtained.

The coal-based carbon quantum dots were tested by a JEM-2100f transmission electron microscope (TEM) equipped with a computer imaging system (the working voltage of the TEM is 200 kV; the point resolution is 0.19 nm; and the line resolution is 0.14 nm). The test details are as follows: (1) An appropriate amount of carbon quantum dot powder was placed into the test tube, and then anhydrous ethanol was added and shaken well to fully dissolve the quantum dot powder in ethanol solution. Then, it was dispersed under the condition of 40 kHz ultrasonication for one hour and static settling for three hour to obtain the supernatant, which was then dropped onto an ultrathin copper grid. After the ethanol was evaporated, the coal-based quantum dots were deposited on the copper grid to form an ultrathin film that was transparent to the electron beam. (2) Find the enrichment region of quantum dots at low magnification and then scan at high magnification to obtain the lattice fringe of the quantum dots. To prevent damage caused by electron beam irradiation, control the current density on the screen to be less than 5 pA/cm^2.

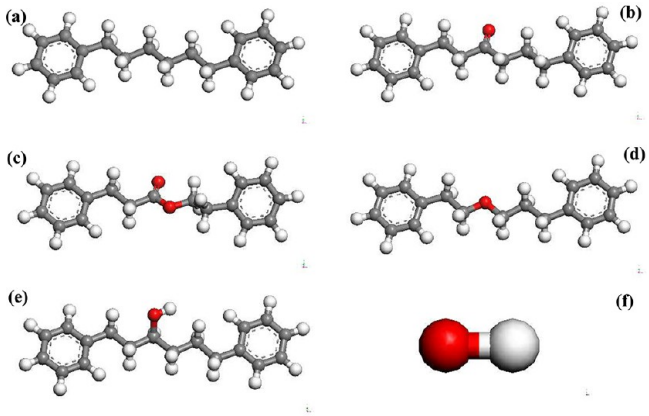

Figure 2. Optimized configuration of coal and hydroxyl radicals: (a) Ar-$(CH_2)_6$-Ar, (b) Ar-$(CH_2)_2$−C = O-$(CH_2)_3$-Ar, (c) Ar-$(CH_2)_2$−COO-$(CH_2)_2$−Ar, (d) Ar-$(CH_2)_2$−O-$(CH_2)_3$-Ar, (e) Ar-$(CH_2)_2$−CHOH-$(CH_2)_3$-Ar, (f) OH•, Red: oxygen; White: hydrogen; gray: carbon.

https://doi.org/10.1021/acsomega.3c06525
ACS Omega 2024, 9, 753−770

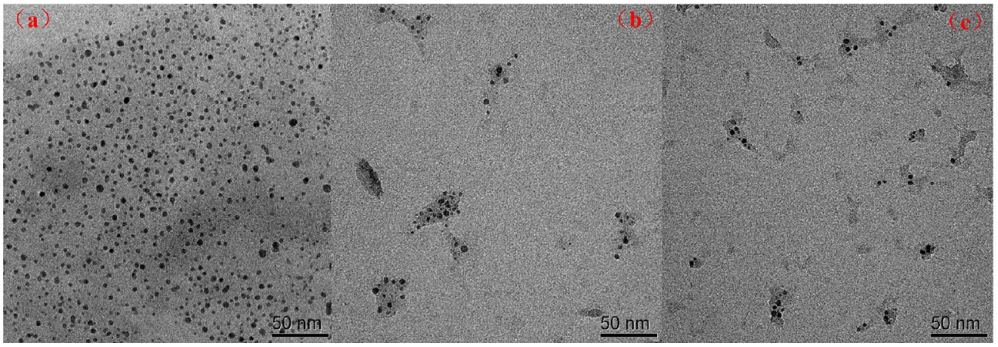

Figure 3. Coal-based carbon quantum dots: (a) subbituminous coal, (b) bituminous coal, and (c) anthracite.

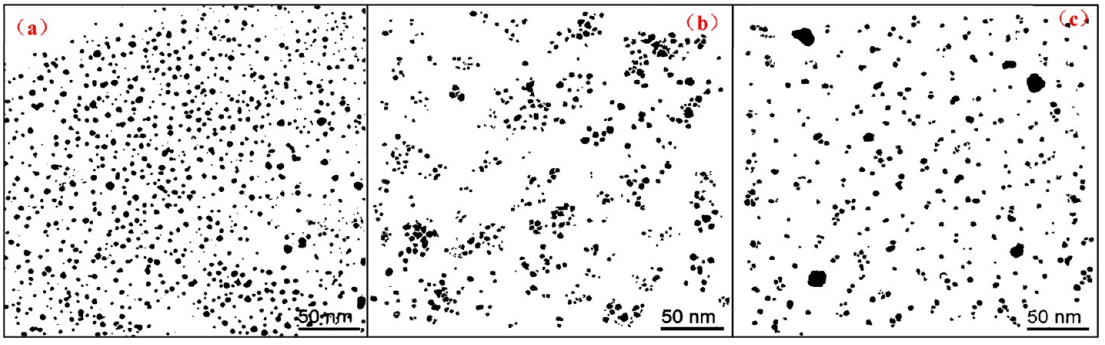

Figure 4. Binary image of coal-based carbon quantum dots: (a) subbituminous coal, (b) bituminous coal, and (c) anthracite.

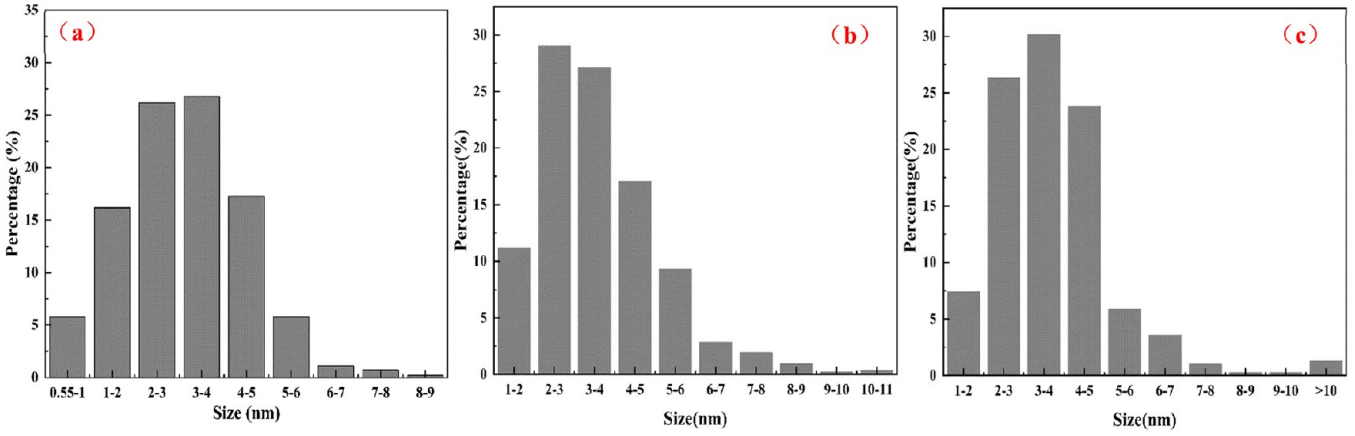

Figure 5. Size distribution of coal-based carbon quantum dots: (a) subbituminous coal, (b) bituminous coal, and (c) anthracite.

2.2. Computational Model and Method. All DFT calculations were performed with the Dmol^3 module integrated with the Materials Studio 2019 software. The exchange correlation term was calculated by the BLYP[29,30] functional, which can be used in strong conjugation systems and radicals[31−37] and is accurate for thermodynamic calculations under the generalized gradient approximation (GGA). If the system contains a single electron or free radicals, check the spin unrestricted option, and use a formal spin initial to set the primary spin.[38] The core treatment adopted the all electron method without special treatment of inner electrons, and all electrons were calculated. The numerical basis group DNP[39] was employed, the global mode was selected for the orbital cutoff scheme, and the calculation accuracy was fine. To ensure the convergence of the SCF process, we set its maximum number of cycles to 500, check the smearing option and set the value to 0.005 Ha.[40]

All models will first be performed with geometry optimization, and the calculation will converge when the energy difference between two adjacent calculation results is less than 10^{-5} Ha, the change in the maximum atomic force is less than 0.002 Ha/Å, and the maximum atomic displacement is less than 0.005 Å. Figure 1 shows the optimized configuration of ozone, oxygen, and water, in which the calculated value of ozone bond length is 1.296 Å and the bond angle is 117.890°, the calculated bond length of oxygen is 1.237 Å, the calculated bond length of water is 0.972 Å, and the bond angle is 103.898°. This result is consistent with the experimental values: the bond length and bond angle of ozone are 1.278 Å and 116.8°,[41] the bond length of oxygen is 1.208 Å,[42] and the bond length and bond angle of water[42] are 0.96 Å and 104.48°, respectively.

Jiang[43] conducted research on the functional groups of coal by FTIR and found that there are absorption peaks of

https://doi.org/10.1021/acsomega.3c06525
ACS Omega 2024, 9, 753−770

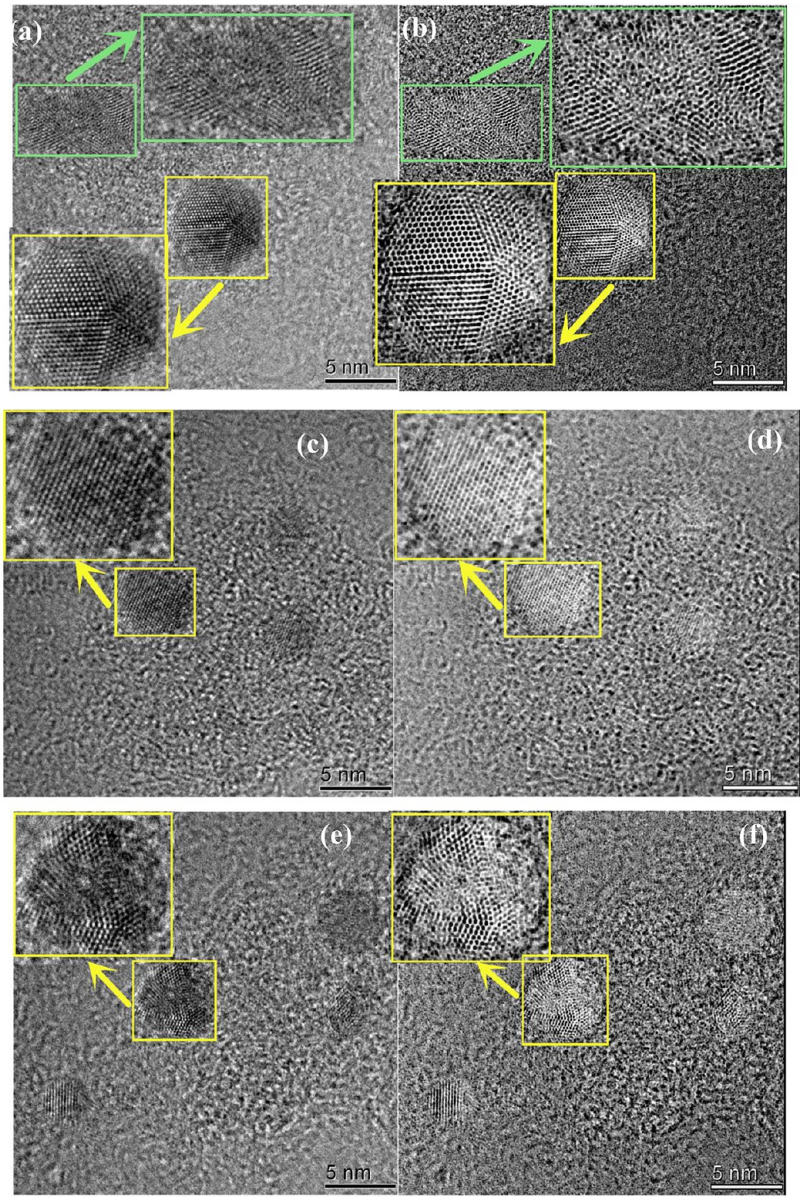

Figure 6. Lattice fringes of coal-based carbon quantum dots: (a, b) subbituminous coal; (c, d) bituminous coal; (e, f) anthracite

Table 1. Frontier Orbital Energy of Coal Molecules, O_3 and OH•

			with O_3		with OH•	
Molecules	HOMO (eV)	LUMO (eV)	ΔE_1 (eV)	ΔE_2 (eV)	ΔE_1 (eV)	ΔE_2 (eV)
Ar−CH2	−5.61	−0.79	0.54	7.02	1.17	5.99
Ar−O−	−5.61	−0.87	0.54	6.94	1.17	5.91
Ar−C═O	−5.55	−1.52	0.60	6.29	1.22	5.25
Ar−C−OH	−5.55	−0.90	0.60	6.91	1.22	5.88
Ar−COO	−5.69	−1.01	0.46	6.80	1.09	5.77
O_3	−7.81	−6.15				
OH•	−6.78	−6.78				

methylene ($-CH_2$) at wavenumbers of 2920 and 2850 cm^{-1}. The average number of methylene carbons in high volatile bituminous, medium volatile bituminous, low volatile bituminous, and semi anthracite is 6.91, 4.9, 0.96, and 0.94, respectively. Wu[44] studied the structural parameters of eight kinds of coal from high volatile bituminous to anthracite by FTIR and peak fitting technology. It was found that the average number of methylene carbons was in the range of 1.48−4.69. To make the article concise, this paper only adopted high volatile bituminous coal as the narrative object, and the number of methylene carbons is 6 ($(4.69 + 6.91)/2 = 5.8 \approx 6$). The simulation study on the oxidation mechanism of medium volatile bituminous coal and low volatile bituminous coal and anthracite is presented in the supplementary document. Because the macromolecular structure calculation of coal by DFT will involve a large number of electrons, and according to the method proposed by Chen[45] and Li,[46] several coal units that can reflect the structural characteristics of coal were constructed, as shown in Figure 2.

Many scholars[47−50] have found that ozone will quickly decompose in water, and a series of chain reactions will occur, resulting in many short-lived species, such as OH•, O_3^-, and O_2^-. Westerhoff[51] pointed out that in all reactants, products, and intermediates, O_3 and OH• can oxidize organic and

https://doi.org/10.1021/acsomega.3c06525
ACS Omega 2024, 9, 753−770

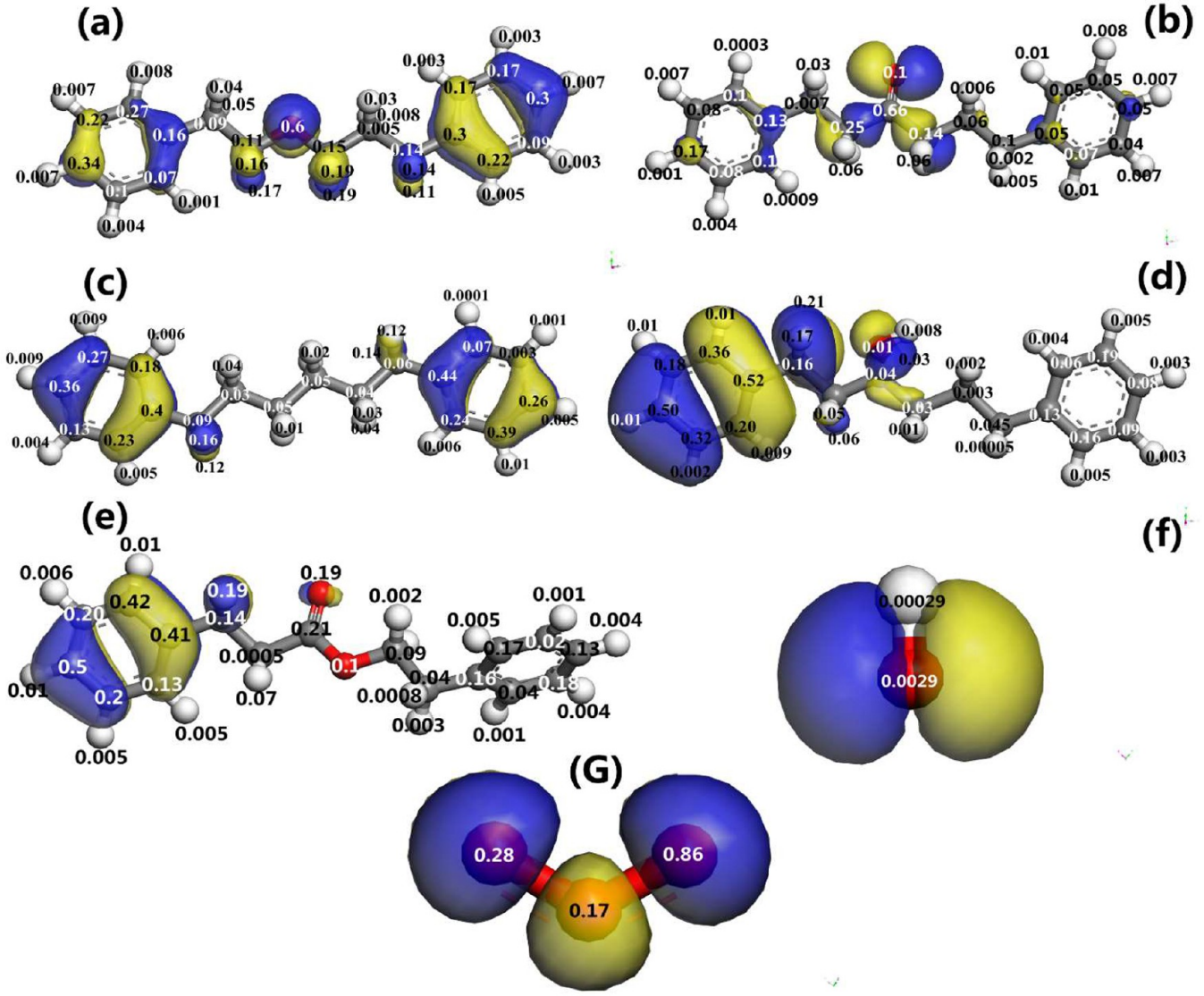

Figure 7. HOMO of coal molecules, LUMO of O_3 and OH•, and orbital coefficients of each atom (blue cloud: the wave function is positive, yellow cloud: the wave function is negative).

inorganic substances in water. Among them, the hydroxyl radical (OH•) is an important reactive oxygen species.[52] From the molecular formula, it is formed by the loss of one electron from the hydroxide radical. It has a very strong oxidizing ability with an oxidation potential of 2.8 V,[53] which is second only to fluorine in natural oxidants. On the other hand, O_3 can selectively react with unsaturated bonds in organic substances but has low reactivity with saturated hydrocarbons.[54] In contrast, OH• has poor oxidation selectivity. To study the oxidation mechanism of ozone on coal, a model of hydroxyl radicals (OH•) was also constructed, as shown in Figure 2f.

The change values of Gibbs free energy and enthalpy before and after the reaction are obtained from Formulas 1 and 2.[55]

$$\Delta G = \Delta H - T\Delta S \quad (1)$$

$$\Delta H = \Delta U - P\Delta V \quad (2)$$

where ΔG and ΔH are the change values of Gibbs free energy and enthalpy, respectively. T is the temperature, ΔS is the entropy change, ΔU is the change in the internal energy of the system, P is the pressure, and ΔV is the change in volume.

3. RESULTS AND DISCUSSION

3.1. HRTEM Results of Coal-Based Carbon Quantum Dots. Figure 3a shows the morphology of carbon quantum dots prepared from subbituminous coal. On the scale of 50 nm, the carbon dots are dense, and Figure 3b and c show carbon quantum dots prepared from bituminous coal and anthracite, respectively. In contrast, they have less quantity and sparse distribution. Therefore, we scanned several different regions under the 50 nm scale to ensure that a sufficient number of carbon quantum dots of bituminous coal and anthracite were obtained and that their size distribution was statistically significant. To facilitate size statistics, we combined carbon quantum dots at different positions into one graph through image processing, obtained the binary graph by MATLAB, and calculated the equivalent diameter distribution of all carbon quantum dots. The results are shown in Figure 4 and Figure 5. To make the article concise, other morphology images of bituminous coal and anthracite that were adopted to generate Figure 4b, c are included in the Supporting Informationt.

The average sizes of all carbon quantum dots in Figure 4a−c are 3.1 3.59, and 3.78 nm, respectively. The morphology of

https://doi.org/10.1021/acsomega.3c06525
ACS Omega 2024, 9, 753−770

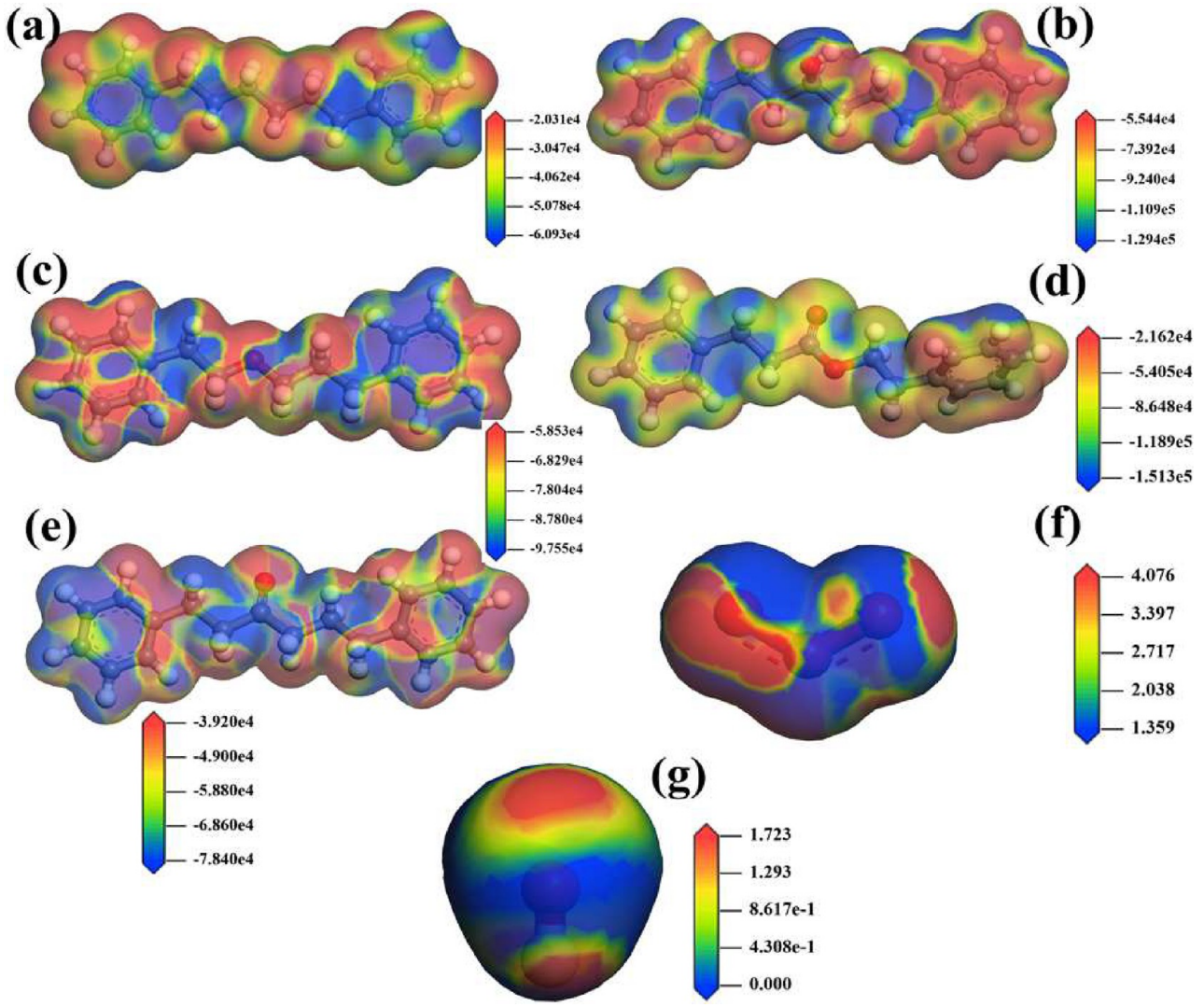

Figure 8. f^- of five coal molecules and f^+ function of O_3 and OH•.

carbon quantum dots shown in Figure 3 and the average size of carbon quantum dots are similar to the results obtained by other scholars.[56−59]

We artificially specified that <2 nm is the small-size carbon quantum dot, 2 nm-6 nm is the medium size, and >6 nm is the large size. As shown in Figure 5a−c, the proportions of small carbon quantum dots in subbituminous coal, bituminous coal, and anthracite are 21.97%, 11.2%, and 7.42%, respectively. The proportions of medium-sized particles are 76.02%, 82.54%, and 86.19%, respectively. The proportions of large-size particles are 2%, 6.26%, and 6.39%, respectively. Thus, with the increase in coal rank, the proportion of small-size carbon quantum dots decreases significantly, the proportion of medium-size and large-size carbon quantum dots increases, and some large-size carbon quantum dots appear in anthracite (>10 nm, Figure 5c).

The study of coal molecular structure has always been the focus and difficulty in the field of coal chemistry, and there is still no unified theory.[60] Many scholars have directly conducted XRD, HRTEM, and ^{13}CNMR studies on the molecular structure of coal. They believe that low-rank coal is mainly composed of basic structural units composed of 1−3 benzene rings connected by side chains.[61] This understanding is one-sided. Therefore, in this study, we randomly selected the carbon quantum dots of three coals and obtained their lattice fringes, revealing the macromolecular structure of the three coals from a visualization point of view. Figure 6a, c, and e are the original pictures of carbon quantum dots of subbituminous coal, bituminous coal, and anthracite, respectively. Image-Pro Plus software was used to perform Gauss, HitGauss and sharpen operations on the three images to reduce noise and improve contrast. Then, a dilation operation is performed to refine the contour of the image. Finally, the inverse operation is performed on all images to obtain Figure 6b, d, and f. The arrow points to an enlarged view of the corresponding carbon quantum dot.

According to Figure 6a and b, after image processing, the internal benzene ring structure is clearly visible, indicating that there are more than 15 × 15 aromatic sheets in the subbituminous coal. Moreover, there are obvious boundaries inside the molecular fragments, which are presumed to be caused by the bending of adjacent aromatic sheets in space. There are a large number of amorphous structures in subbituminous coal, such as the part in the green box. The atoms inside are arranged irregularly, which is a spatially highly cross-linked macromolecular structure. Figure 6c and d show

https://doi.org/10.1021/acsomega.3c06525
ACS Omega 2024, 9, 753−770

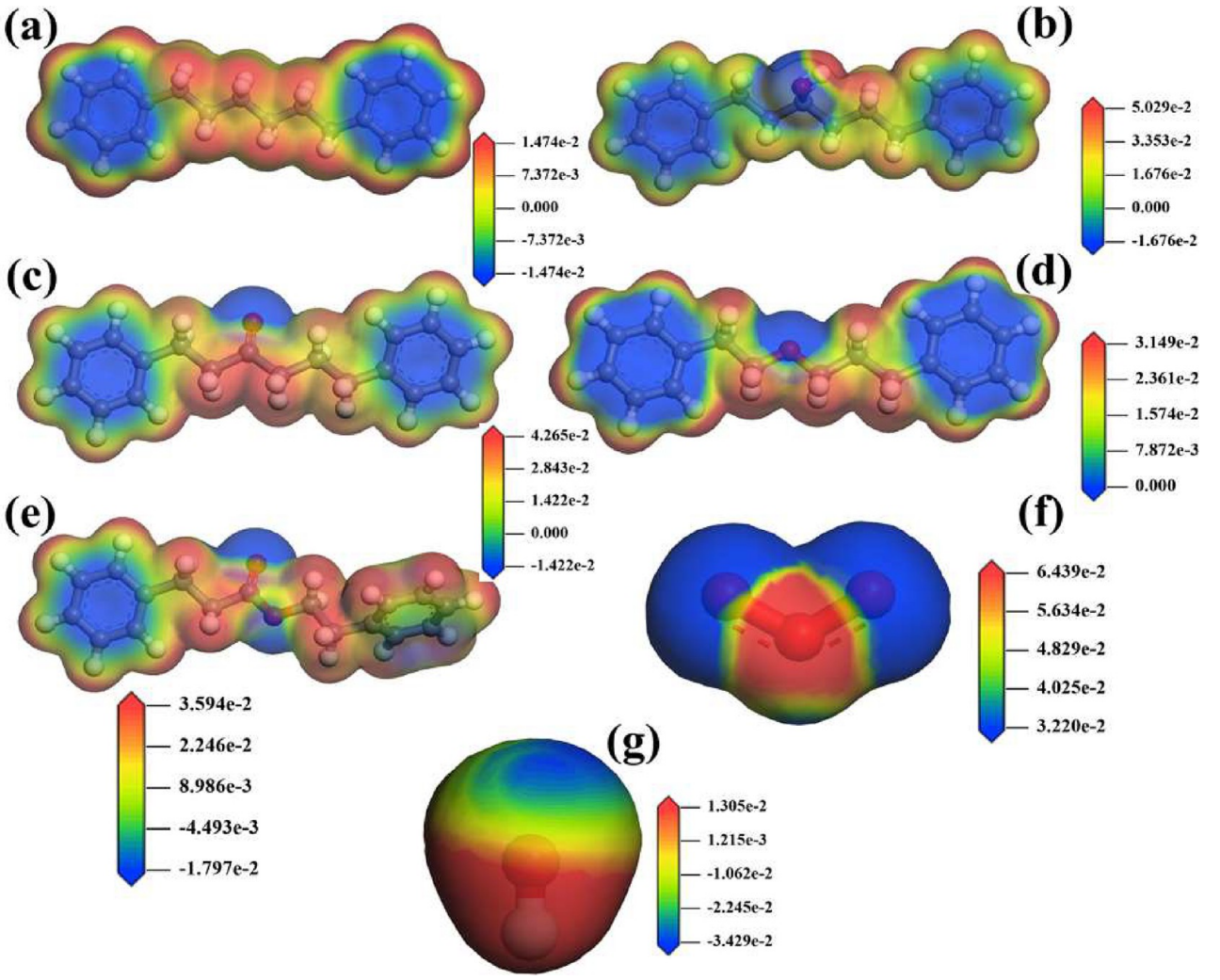

Figure 9. Electrostatic potentials of five coal molecules and of the O_3 and OH•.

the lattice fringe of a molecular fragment in bituminous coal, similar to subbituminous coal. The part in the yellow box is also the neatly arranged benzene ring structure, and the size is more than 15 × 15. Figure 6e and f are lattice fringes of molecular fragments in anthracite, and there are both regular and amorphous components in the field of view. The part in the yellow box is a symbiont of regular structure and amorphous components.

In summary, the morphology and lattice fringes of coal-based carbon quantum dots obtained after coal oxidized by ozone were characterized. Different from various spectral methods in which the structure of coal is speculated according to the test results, in this study, the atomic arrangement in coal molecular fragments is more accurate and reliable and can be directly observed from the perspective of visualization. To study the surface oxidation mechanism, the results of density functional theory calculations were also analyzed as followed.

3.2. Electronic Properties of Coal, Ozone, and Hydroxyl Radicals. The essence of a chemical reaction is the electron transfer. Therefore, clarifying the electronic properties of reactants is the premise of studying chemical reactions. According to Fukui's frontier orbital theory,[62] when the frontier orbitals of two molecules meet the principles of similar energy, consistent symmetry and maximum overlap, chemical reactions easily occur. Therefore, the possible reaction sites can be determined according to the frontier orbit. The Fukui function[63] can predict the ability of molecules to suffer "nucleophilic attack," "electrophilic attack," and "free radical attack." The larger the Fukui function, the easier the reaction. This parameter can directly determine the nucleophilic, electrophilic, and free radical reaction sites. The electrostatic potential represents the molecular surface potential, which can directly judge the position of the electron-rich and electron-poor regions, and electron-rich regions may lose electrons. Therefore, this parameter can also reveal the potential reaction sites.

3.2.1. Frontier Orbital. The energy difference of the frontier orbit is obtained from eqs 3 and 4. Table 1 shows that the highest occupied orbit (HOMO) energies of the five simplified coal molecules have little difference and are distributed in the range −5.56 to 5.69 eV. In contrast, the energy of the lowest unoccupied molecular orbital (LUMO) has a certain difference, which is distributed in the range −0.79−1.52 eV. The absolute values of the frontier orbit energy difference between the coal molecular model and the O_3 and OH• are calculated. The results show that the energy of the HOMO of coal molecules is less different from that of O_3 and OH• LUMO. According to the condition of the orbital energy approximation, it is considered that the LUMO orbitals of O_3 and OH• preferentially overlap with the HOMO orbitals of coal

https://doi.org/10.1021/acsomega.3c06525
ACS Omega 2024, 9, 753−770

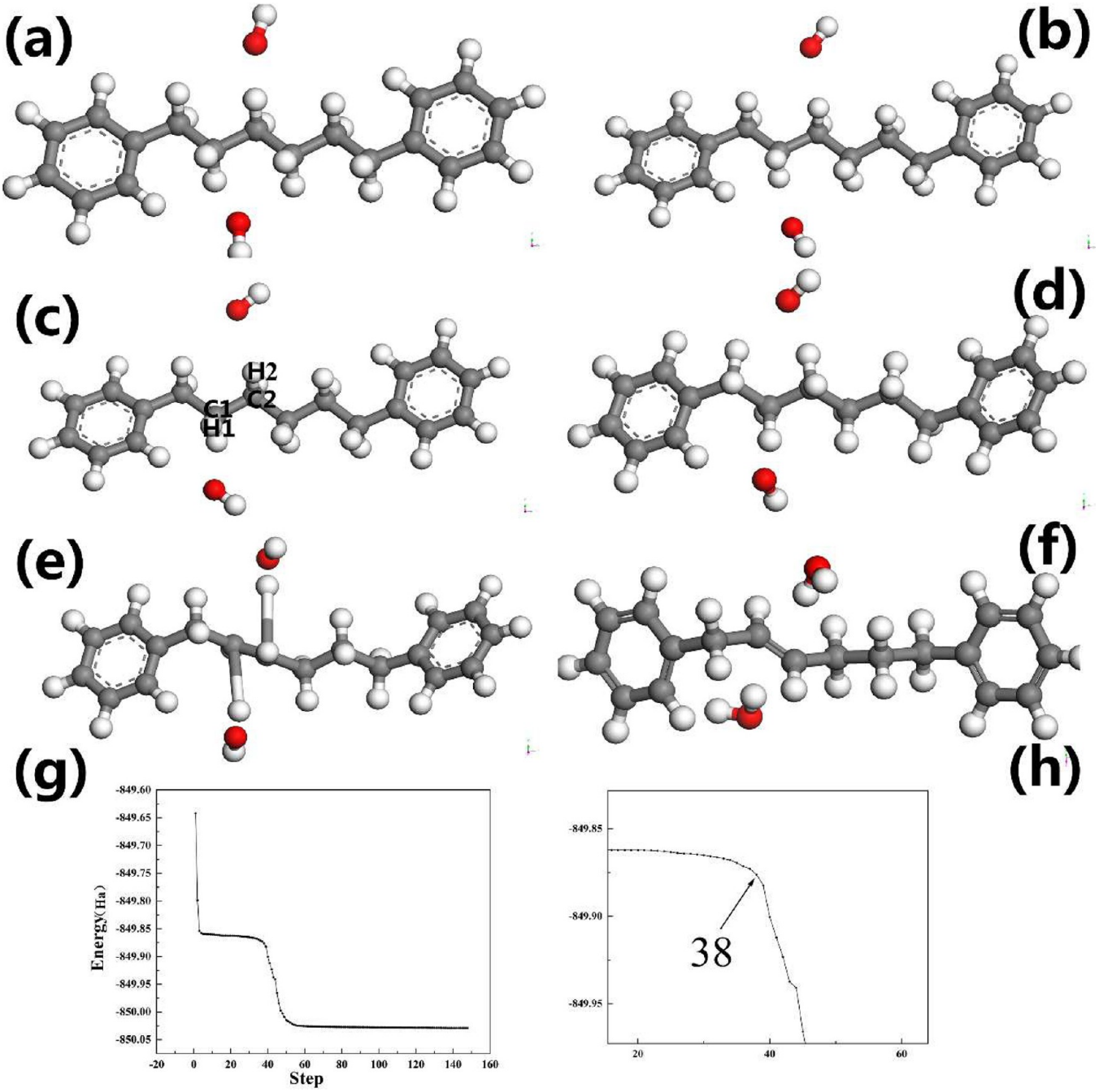

Figure 10. Interaction process between coal molecules and OH•: (a) initial configuration, (b) optimization step 15, (c) optimization step 22, (d) optimization step 38, (e) optimization step 61, (f) equilibrium configuration, (g) energy curve, and (h) local amplification of energy curve.

molecules. Combined with the cloud diagram of the frontier orbital, the reaction sites can be judged preliminarily.

$$\Delta E_1 = |E_{HOMO}^{coal} - E_{LUMO}^{O_3 \text{ or } OH\bullet}| \quad (3)$$

$$\Delta E_2 = |E_{LUMO}^{coal} - E_{HOMO}^{O_3 \text{ or } OH\bullet}| \quad (4)$$

In Dmol[3], the molecular orbital is a linear combination of atomic orbitals, so the absolute values of all atomic orbital coefficients were calculated. The larger the value is, the greater the contribution of the atom to the Frontier orbital.[64] Figure 7 shows that the difference in oxygen-containing functional groups leads to the difference in the frontier orbitals of coal molecules. HOMO in Figure 7a is distributed throughout the molecule, and the orbital coefficient of the oxygen atom on the −O− functional group is the largest (0.6). Therefore, this site has the highest potential reaction activity and is vulnerable to electrophilic attack and loss of electrons. HOMO in Figure 7b is mainly concentrated on C═O, and carbonyl carbon (orbital coefficient of 0.66) and oxygen (orbital coefficient of 0.1) have high reaction activity. HOMO in Figure 7c is mainly concentrated on benzene, and the hydrogen connected to benzene also has a relatively large orbital coefficient and certain reaction activity. HOMO in Figure 7d is distributed on −OH and the benzene close to it, and the hydrogen atom between them also has a large orbital coefficient, indicating that this is a potential reaction site. HOMO in Figure 7e is distributed on

https://doi.org/10.1021/acsomega.3c06525
ACS Omega 2024, 9, 753−770

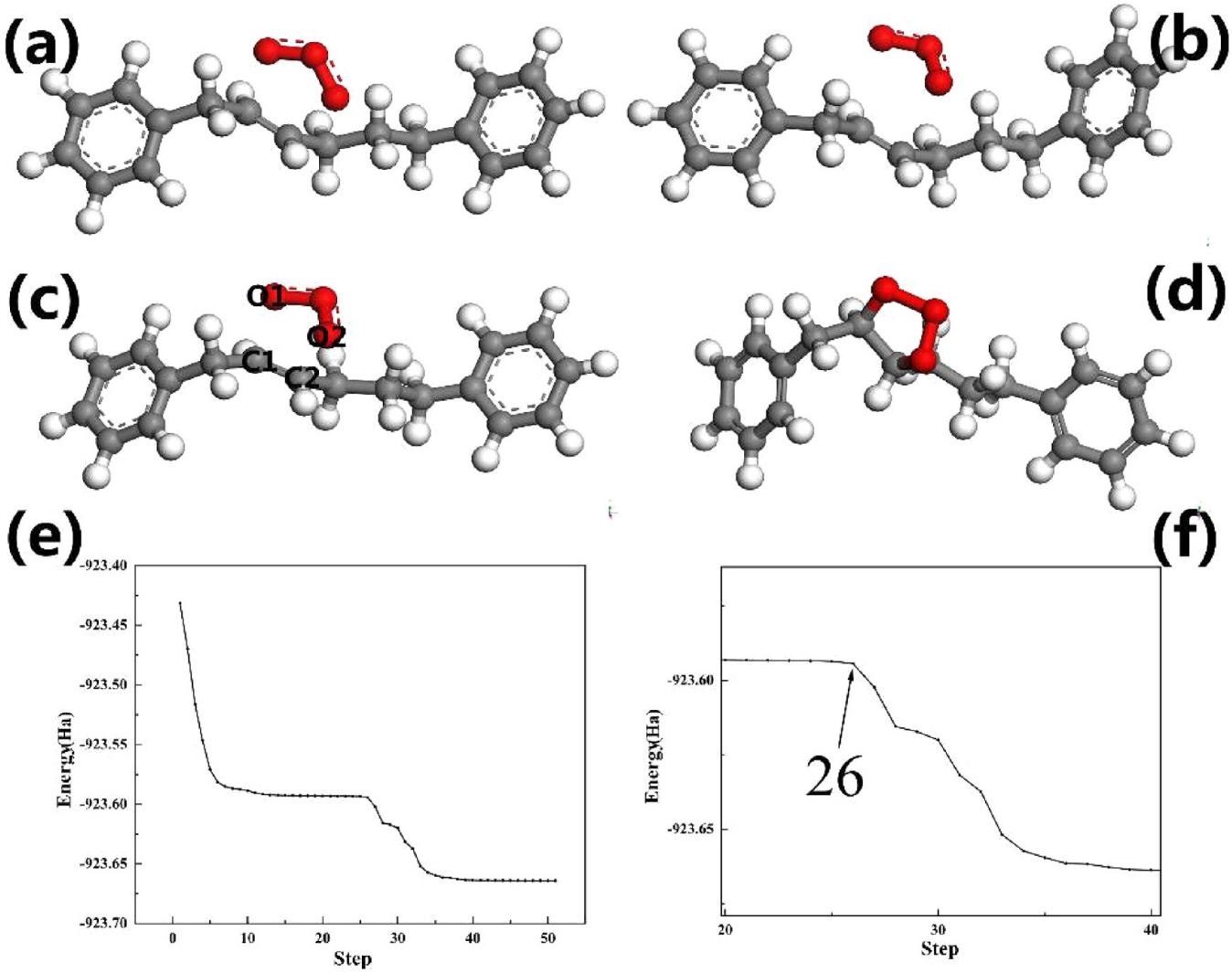

Figure 11. Interaction process of Ar−CH_2−CH═CH−$(CH_2)_3$−Ar and O_3: (a) initial configuration, (b) step 8, (c) step 26, (d) equilibrium configuration, (e) energy curve, and (f) local amplification of energy curve.

the −O−C═O− functional group and CH_2 connected with the benzene on the left, and the orbital coefficients of all atoms on both of them are relatively large (0.1−0.21), so they are the active sites of the coal molecule. As shown in Figure 7 f and g, in LUMO of OH•, the orbital coefficient of the O atom is 0.0029, which is ten times that of hydrogen. Therefore, the active site of OH•. In O_3, the orbital coefficient of the right O atom is 0.86, so the reaction activity is the highest. The possible reaction sites of all reactants are defined through frontier orbital theory. Next, combined with the Fukui function, the possible reaction sites are further analyzed to provide theoretical guidance for the construction of the initial reaction model.

3.2.2. Fukui Function and Electrostatic Potential. According to the results of frontier orbitals, the LUMO energy of O_3 and OH• is similar to the HOMO energy of coal molecules. Thus, in their possible reactions, coal molecules lose electrons and O_3 or OH• gain electrons. Then, the electrophilic index f^- of coal with different oxygen-containing functional groups and the nucleophilic index f^+ of O_3 and OH• were calculated, as shown in Figure 8. When there is no oxygen atom in the side chain, the larger f^- value (red) is almost distributed near the carbon and hydrogen atoms, indicating that CH_2 is vulnerable to electrophilic attack and loses electrons. Figure 8 shows that due to the existence of hydroxyl groups, in addition to hydrogen in CH_2, the hydrogen on some benzene also has a high f^- index, and these sites are vulnerable to electrophilic attack and lose electrons. In Figure 8c, because of the existence of −O−, the electron loss ability of CH_2 at the left meta position tends to decrease. In Figure 8d, the electron loss ability of CH_2 in the left position of −O−C═O is further reduced. Figure 8e shows that the f^- of the benzene on the left decreases significantly, and the electron loss ability of some hydrocarbon atoms in CH_2 also decreases. In conclusion, CH_2 has a high nucleophilic index f^- and a certain reactivity, which makes it easy to lose electrons. At the same time, the introduction of oxygen-containing functional groups significantly changed the f^- distribution on the surface of coal molecules, indicating that oxygen-containing functional groups have an important impact on the properties of coal, and almost all oxygen-containing functional groups have a high f^- index. Figure 8f and g show that the oxygen atoms at both ends of the O_3 molecule are more vulnerable to nucleophilic attack to obtain electrons, and the oxygen atom and hydrogen atom of OH• have a high nucleophilic index at the same time; therefore, it is easy to obtain electrons.

https://doi.org/10.1021/acsomega.3c06525
ACS Omega 2024, 9, 753−770

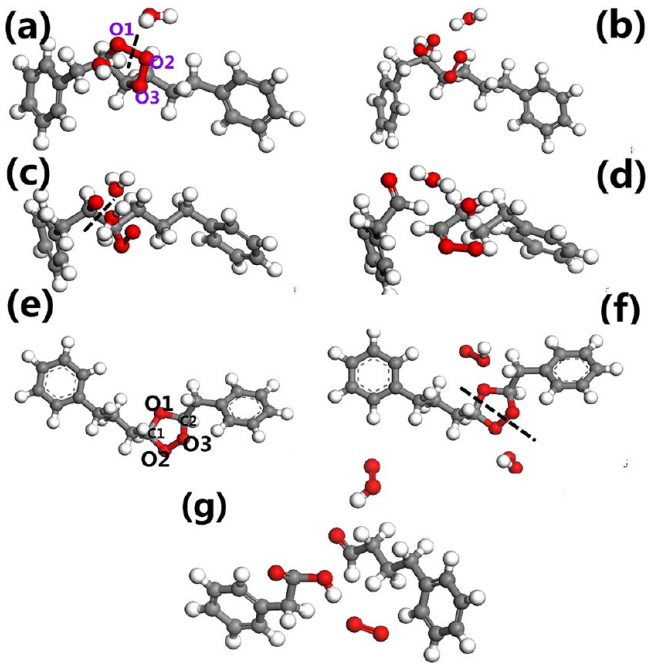

Figure 12. Cracking reaction process of POZ and SOZ: (a) initial configuration, (b) O1−O2 breaking in POZ, (c) and (d) C1−C2 breaking in POZ, (e) SOZ, (f) initial configuration of SOZ and HO_2•, (g) cleavage products of SOZ.

The physical meaning of the electrostatic potential is the work needed to move the unit positive charge from infinity to this position. It is used to describe the interaction energy between the unit positive charge at a certain site and the system and can reflect the distribution of molecular surface charge.[65] Figure 9a−e shows that the electrons on the large π bond of benzene are distributed in the whole benzene ring region. The electrostatic potential near the oxygen atoms of all oxygen-containing functional groups is low, which is an electron rich region. Compared with hydrogen, carbon in CH_2 has a lower electrostatic potential value. In conclusion, oxygen atoms are vulnerable to electrophilic attack and lose electrons, and benzene rings are also vulnerable to electrophilic attack. The electrostatic potentials of H atoms outside almost all are large, indicating that H is a bare nucleus. Although the electrostatic potential of oxygen atoms at both ends of the atoms of the O_3 is low, it is still positive; therefore, it is vulnerable to nucleophilic attack. The oxygen atom in OH• has low electrostatic potential and is an electron-rich region.

The active sites of each molecule were determined by analyzing the frontier orbitals, Fukui function, and electrostatic potential of coal molecules, O_3 and OH•. This not only defines their reactivity but also provides theoretical guidance for the construction of the initial model in the following study.

3.3. Reaction Mechanism of OH• and O_3 with Ar-$(CH_2)_6$-Ar. As mentioned above, O_3 has a low reaction activity with saturated alkanes but high reaction activity and selectivity with unsaturated alkanes (olefins and alkynes). Therefore, the initial adsorption configuration of OH• and the coal molecules was constructed to explore their adsorption and chemical reaction mechanism.

3.3.1. Reaction Process. 3.3.1.1. Reaction of OH• with Ar-$(CH_2)_6$-Ar. First, according to Section 3.2, the initial model was constructed, as shown in Figure 10a, where the initial bond length of C1−H1 is 1.121 Å. Figure 10b shows that in the early optimization process, the two OH• are constantly adjusting the direction while keeping away from the coal molecules. At this time, the bond lengths between C1−H1 and C2−H2 are basically maintained. When the optimization proceeds to step 22, OH• is constantly approaching Ar-$(CH_2)_6$-Ar, and the C1−H1 bond length increases sharply to 1.264 Å in step 39, indicating that H1 has already shown a state of shedding. Therefore, it can be seen that the first 38 steps of geometry optimization are the physical adsorption process of OH• and Ar-$(CH_2)_6$-Ar (this can also be obtained from the energy curve Figure 10g and h: the energy curve sharply decreases after step 38), the adsorption energy is −9.41 kcal/mol, and this physical adsorption process is a prerequisite for the chemical reaction. When the sequence is optimized to step 61 (Figure 10e), the distance between C1 and H1 has reached 2.61 Å, which has actually broken, and the distance between C2 and H2 is 2.64 Å and has also fallen off the carbon skeleton. In summary, as shown in Figure 10f, the reaction between OH• and Ar-$(CH_2)_6$-Ar is finally shown as OH• taking two hydrogen atoms from Ar-$(CH_2)_6$-Ar and generating two H_2O atoms. Then, the bond between C1 and C2 exhibits the nature of a double bond and reacts with O_3.

3.3.1.2. Reaction of O_3 with Ar−CH_2−CH═CH−$(CH_2)_3$−Ar. The reaction process of O_3 and Ar−CH_2−CH═CH−$(CH_2)_3$−Ar was calculated by the DFT method (Figure 11), and the reaction mechanism was analyzed.

The ozone was placed vertically directly above the double bond in the Ar−CH_2−CH═CH−$(CH_2)_3$−Ar molecule to obtain the initial configuration. The initial distances between O1 and C1 and between O2 and C2 in Figure 11 are 1.895 and 1.909 Å, respectively, and the maximum value of the two-atom bond length is 1.15 times the sum of the covalent radius according to the default value in Materials Studio 2019. For C and O, the value is 1.74 Å, which is smaller than the carbon−oxygen atom spacing in the initial configuration, indicating that there is no chemical bond between ozone and Ar−CH2−CH═C−$(CH_2)_3$-Ar molecules in the initial configuration. When the optimization proceeds to step 8 (Figure 11(b)), the ozone molecule gradually moves away from Ar−CH_2−CH═CH−$(CH_2)_3$−Ar and adjusts its orientation constantly. The distances between O1 and C1 and between O2 and C2 reached their maximum values at 2.772 and 2.734 Å, respectively. Subsequently, under the action of physical adsorption, the distance is constantly shrinking, and in step 26 (Figure 11c), O_3 and C═C undergo an addition reaction

Table 2. Energy of OH•, Ar-$(CH_2)_6$-Ar, and Products

Molecules	G(kcal/mol)	H(kcal/mol)	E_t(kcal/mol)	ΔH(kcal/mol)	ΔG(kcal/mol)
Ar−$(CH_2)_6$−Ar	185.44	227.48	−438 668.45	−104.05	−105.28
OH•	−5.12	7.18	−47 537.60		
H_2O	1.51	15.38	−47 971.03		
Ar−CH_2−CH═CH−$(CH_2)_3$−Ar	172.36	212.48	−437 907.06		

https://doi.org/10.1021/acsomega.3c06525
ACS Omega 2024, 9, 753−770

Table 3. Energy of Ozone, Ar−CH_2−CH═CH−$(CH_2)_3$−Ar, and Products

Molecules	G(kcal/mol)	H(kcal/mol)	E_t(kcal/mol)	ΔH(kcal/mol)	ΔG(kcal/mol)
Ar−CH_2−CH═CH−$(CH_2)_3$−Ar	172.36	212.48	−437 907.06	−40.13	−27.59
O_3	−11.02	6.45	−141 519.65		
POZ	176.55	221.60	−579 469.51		

Table 4. Energy of POZ and Products

Molecules	G(kcal/mol)	H(kcal/mol)	E_t(kcal/mol)	ΔH(kcal/mol)	ΔG(kcal/mol)
POZ	176.55	221.60	−579 469.51	−93.36	−105.17
CI	98.70	128.92	−338 044.80		
Ar−CH_2CHO	63.15	89.80	−241 515.18		

Table 5. Energy of SOZ, HO_2•, and Products

Molecules	G(kcal/mol)	H(kcal/mol)	E_t(kcal/mol)	ΔH(kcal/mol)	ΔG(kcal/mol)
SOZ	178.08	222.54	−579524.24	−71.81	−87.08
HO_2•	−6.13	10.09	−94739.10		
Ar−$(CH_2)_3$−CHO	94.34	126.36	−290839.31		
O_2	−10.19	4.20	−94369.20		
Ar−CH_2COOH	68.12	97.65	−289122.21		

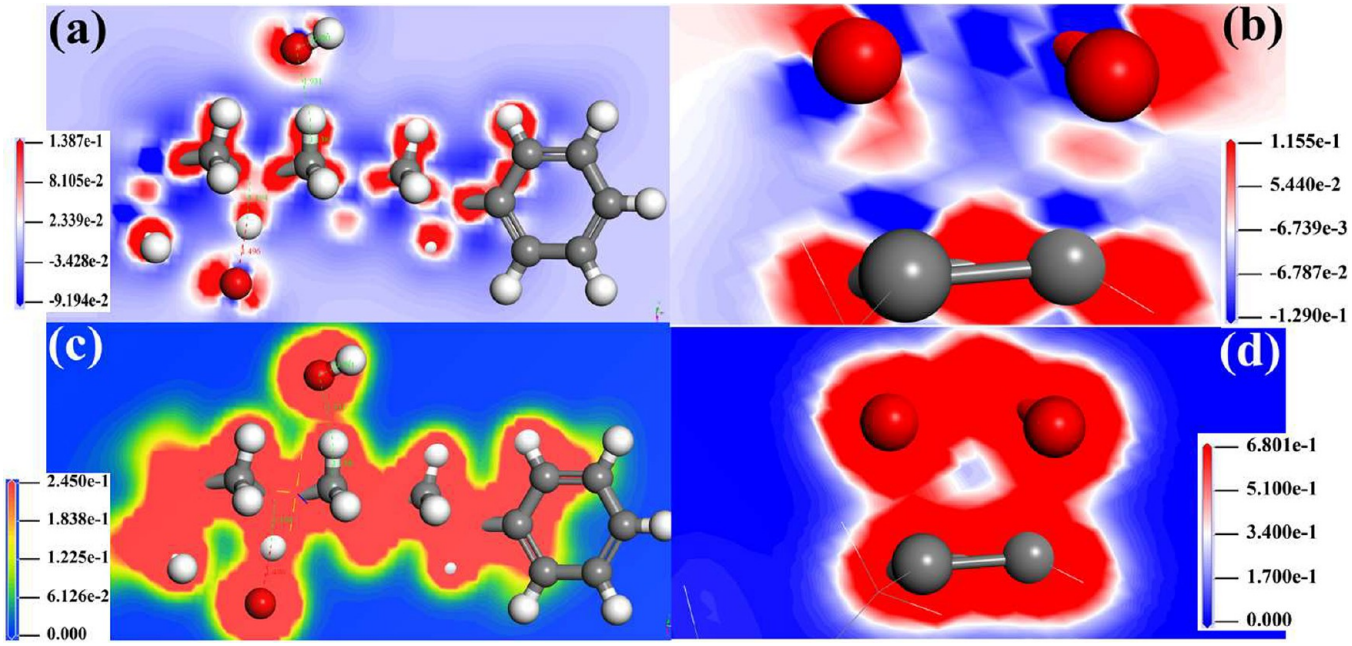

Figure 13. (a) Deformation density after adsorption of OH• and Ar−$(CH_2)_6$−Ar, (b) deformation density after adsorption of O_3 and Ar−CH_2−CH═CH−$(CH_2)_3$−Ar, (c) total electron density after adsorption of OH• and Ar−$(CH_2)_6$−Ar, (d) total electron density after adsorption of O_3 and Ar−CH_2−CH═CH−$(CH_2)_3$−Ar.

to obtain the primary ozonide—POZ, as shown in Figure 11d. Similarly, in Figure 11e and f, the energy of the system has undergone a breakover in step 26, so this point is where the chemical reaction begins. Thus, the first 26 steps are considered to be a physical adsorption process, and the adsorption energy is −12.55 kcal/mol. A large number of studies have shown that POZ is unstable. The DFT calculation results directly support this view; because of the presence of water, the O−O and C−C bonds of POZ will break at the positions shown by the black dashed lines in Figure 12a and c, forming a carbonyl oxide (CI) and an aldehyde compound (Figure 12d), and then the two will recombine to form the ozone secondary oxide SOZ. (Figure 12e). In the experiments of coal oxidized by ozone, the interaction of ozone and water will produce hydrogen superoxide (HO_2•), which can be regarded as the formation of hydrogen peroxide losing one hydrogen atom, so it is also called the hydrogen peroxide radical. It has strong oxidizing properties. The oxidizing property of hydrogen peroxide is mainly reflected by hydrogen superoxide. Therefore, the initial reaction model of HO_2• and SOZ is constructed (Figure 12f). According to the DFT results, the bonds are broken, as shown by the black dotted line in Figure 12f, and the bonds between the atoms of O1−C1 and O2−O3 is broken. At the same time, O2 will capture the hydrogen atom of HO_2•, and finally, two compounds containing carboxyl and aldehyde groups will be produced. The hydrogen peroxide radical loses one H atom and escapes in the form of oxygen. The whole reaction process is shown in

https://doi.org/10.1021/acsomega.3c06525
ACS Omega 2024, 9, 753−770

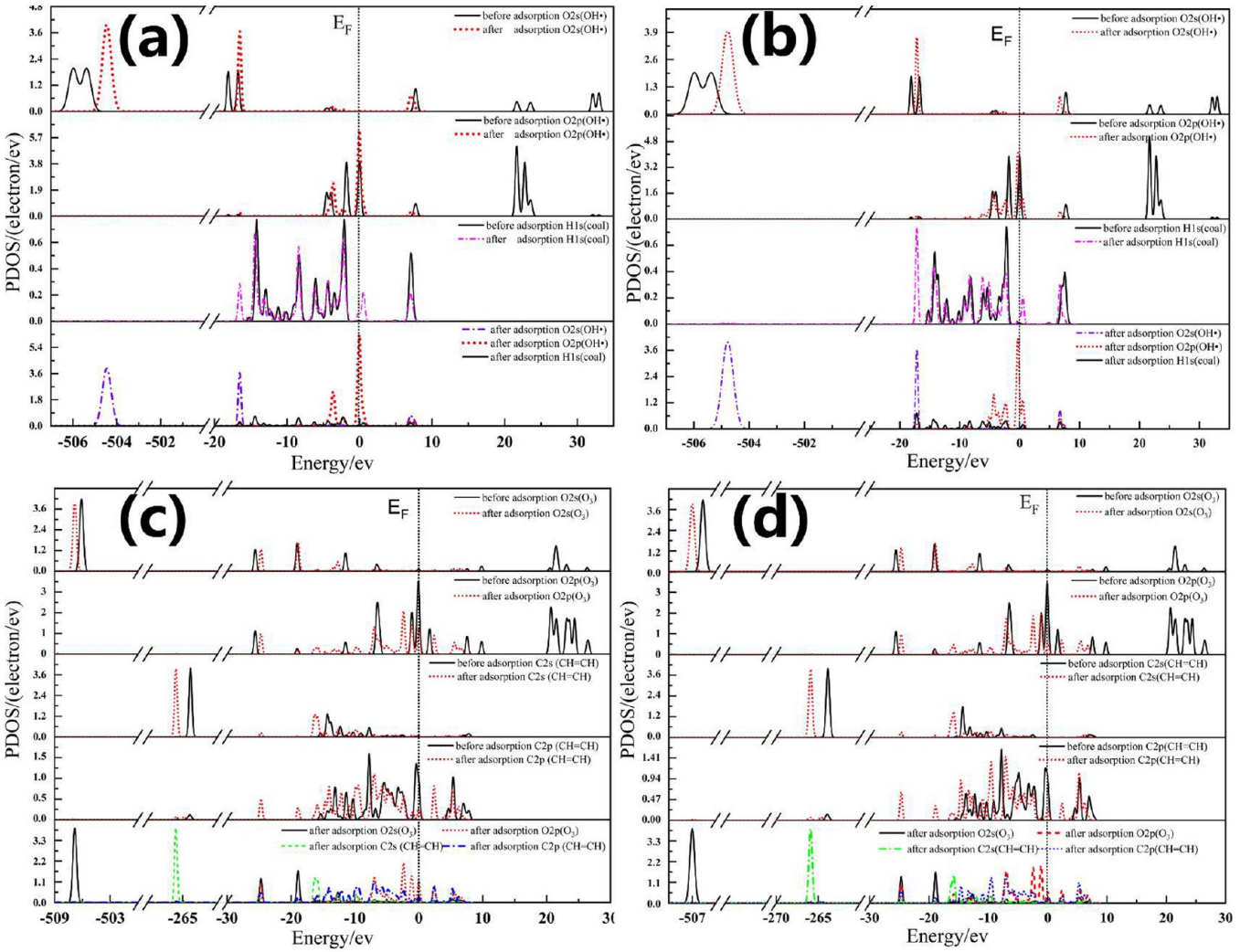

Figure 14. Density of states (a) O41 and H29, (b) O43 and H27, (c) O39 and C8, (d) O41 and C9.

Figure 12. At this point, the C═C bond was completely broken, and Ar−$(CH_2)_6$−Ar generated two small molecules, Ar−CH_2COOH and Ar−$(CH_2)_3$−CHO.

3.3.2. Energy Change during the Reaction. Although the bond breaking process of coal oxidized by ozone is preliminarily defined through the DFT study above, since the reaction is carried out at normal temperature and pressure, whether the above reactions can occur spontaneously needs to be judged from the perspective of thermodynamics. Therefore, ΔG, ΔH, and the energy of the system in all reactions were calculated according to eqs 5 and 6, and the results are shown in Tables 2−5.

$$\Delta G = G_{pro} + E_{tpro} - (G_{rea} + E_{trea}) \quad (5)$$

$$\Delta H = H_{pro} + E_{tpro} - (H_{rea} + E_{trea}) \quad (6)$$

where G_{pro} and G_{rea} are the Gibbs free energy of products and reactants, respectively, and H_{pro} and H_{rea} are the enthalpy of products and reactants, respectively. E_{tpro} is the total electron energy of the products, and E_{trea} is the total electron energy of the reactants.

According to Tables 2−5, the ΔG of all reactions is in the range of −105.28 kcal/mol~-27.59 kcal/mol, and the ΔH is in the range of −104.05 kcal/mol to −40.13 kcal/mol. Therefore, the above reactions can occur spontaneously at normal temperatures and pressures, and they are exothermic reactions. Among them, the decomposition of POZ and the oxidation reaction of OH• with Ar−$(CH_2)_6$− Ar are intense exothermic reactions.

3.3.3. Population Analysis and Charge Density. For ease of expression, all atoms in the two systems are numbered, as shown in Figure 15. And the number of atoms in Figure 15 is only used for population analysis, charge density, and analysis of density of state. Tables 6 and 7 show the charge distribution of each atom before and after physical adsorption of OH• and Ar−$(CH_2)_6$−Ar, O_3 and Ar−CH_2−CH═CH−$(CH_2)_3$−Ar, respectively. Δcharges is the difference between the Mulliken charges of an atom in the system after and before adsorption. The tables show that the Mulliken charge of each atom changes to varying degrees after adsorption because orbital overlap and charge transfer occur when the adsorbate (OH•, O_3) is close to the adsorbent (Ar-$(CH_2)_6$−Ar, Ar−CH_2−CH═CH−$(CH_2)_3$−Ar), and electron redistribution occurs in the system that loses or obtains electrons. The charge changes of H27, H29, O41 and O43 in Table 6 are 0.206, 0.123, −0.236, and −0.252, respectively, which are significantly greater than those of other atoms in the system. The charges of H27 and H29 increased after adsorption, indicating that they lost electrons, while the charges of O41 and O43 decreased, indicating that they obtained electrons. Similarly, in

https://doi.org/10.1021/acsomega.3c06525
ACS Omega 2024, 9, 753−770

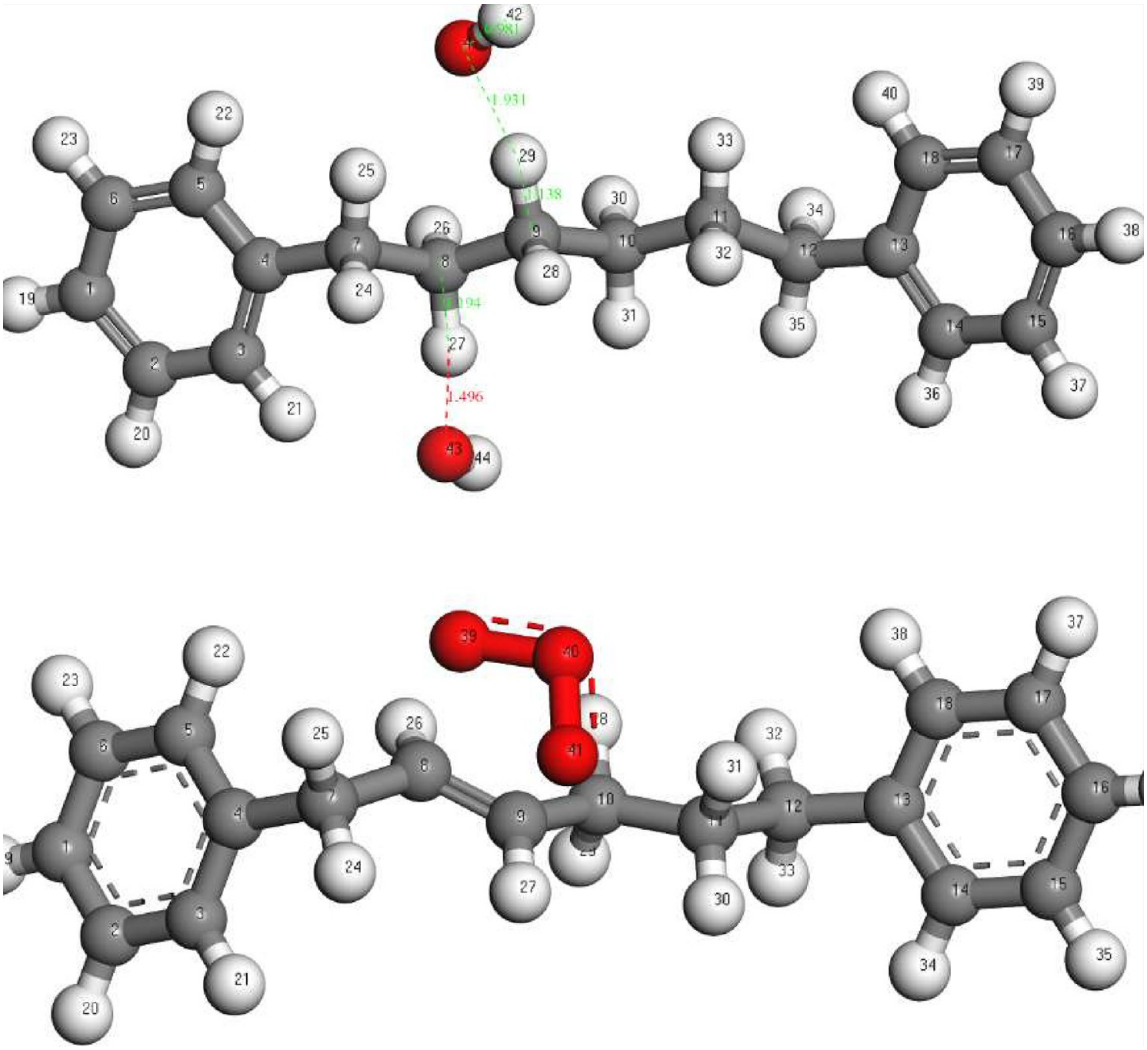

Figure 15. Atomic numbering details.

Table 7, the charge changes after adsorption of C8, C9, O39, O40 and O41 are 0.122, 0.113, −0.159, −0.21 and −0.149, respectively, and all C atoms lose electrons and all O atoms obtain electrons. According to the Mulliken charge of atoms before and after adsorption, it can be easily concluded that the main sites of physical adsorption are H27 and H29 on Ar-$(CH_2)_6$-Ar and C8 and C9 on Ar−CH_2−CH═CH−$(CH_2)_3$−Ar.

Figure 13 illustrates a slice diagram of the charge density diagram of the two systems after adsorption. Between OH• and H27 and H29 in Ar−$(CH_2)_6$−Ar, the change in the electron density around the oxygen atom is positive, indicating that the number of electrons around them increases significantly. The change in electron density outside H27 and H29 is negative, indicating that the electron density around them decreases. Similarly, in Figure 13b, the deformation density outside of O39 and O41 in O_3 is positive, so the electron density increases, and the deformation density outside C8 and C9 is negative; both lose electrons. In the total electron density diagrams shown in Figure 13c and d, the oxygen atoms in OH• and O_3 have obvious electron cloud overlap with the H atoms in Ar-$(CH_2)_6$-Ar and the C atoms on Ar−CH_2−CH═CH−$(CH_2)_3$−Ar, respectively. This phenomenon shows that there is a strong electron interaction between the adsorbate and adsorbent in the two systems, which lays the foundation for the next chemical reaction (bond breaking). The calculated results here are consistent with the conclusion of frontier orbital analysis: coal molecules lose electrons, while OH• and O_3 gain electrons.

3.3.4. Density of States. Figure 14 shows the partial density of states with atoms at the reaction sites before and after the adsorption of OH• on Ar−$(CH_2)_6$−Ar and O_3 on Ar−CH_2−CH═CH−$(CH_2)_3$−Ar. The Fermi level E_F was set to 0 eV. In Figure 14a, the 2 s and 2p orbitals of OH• are concentrated in several specific energy levels, indicating that the electron is strongly localized. The Fermi level passes through the 2p orbital of the oxygen atom; thus, the 2p orbital of the oxygen atom in OH• has high reaction activity. After adsorption, the energy levels of the 2 s orbital at −505.9 eV and −505.4 eV of the oxygen atom in (OH•) are combined into a single strong peak at −504.5 eV. Similarly, the peaks at −18.1 eV and −16.7 eV are combined into a single peak at −16.4 eV. The energy levels at 21.7 eV, 23.6 eV, and 31.8−33.6 eV above the Fermi level disappear. After adsorption, the energy levels of the O 2p orbital at −1.85 and 21.2−24.2 eV disappear, while the density of states at E_F increases significantly.

The energy level distribution range and intensity of the 1 s orbital of the hydrogen atom change little, but new energy

https://doi.org/10.1021/acsomega.3c06525
ACS Omega 2024, 9, 753−770

Table 6. Mulliken Charges of OH• and Ar−$(CH_2)_6$−Ar before and after Adsorption

Atoms	Before adsorption	After adsorption	Δ charges
C1	−0.047	−0.039	0.008
C2	−0.036	−0.03	0.006
C3	−0.055	−0.061	−0.006
C4	0.059	0.068	0.009
C5	−0.05	−0.047	0.003
C6	−0.034	−0.029	0.005
C7	−0.119	−0.162	−0.043
C8	−0.11	−0.152	−0.042
C9	−0.086	−0.128	−0.042
C10	−0.086	−0.096	−0.01
C11	−0.11	−0.088	0.022
C12	−0.119	−0.126	−0.007
C13	0.059	0.069	0.01
C14	−0.049	−0.043	0.006
C15	−0.034	−0.028	0.006
C16	−0.047	−0.042	0.005
C17	−0.036	−0.028	0.008
C18	−0.055	−0.049	0.006
H19	0.03	0.039	0.009
H20	0.031	0.041	0.01
H21	0.035	0.099	0.064
H22	0.026	0.055	0.029
H23	0.031	0.042	0.011
H24	0.059	0.074	0.015
H25	0.064	0.131	0.067
H26	0.056	0.06	0.004
H27	**0.053**	**0.259**	**0.206**
H28	0.046	0.059	0.013
H29	**0.045**	**0.168**	**0.123**
H30	0.046	0.049	0.003
H31	0.045	0.056	0.011
H32	0.056	0.054	−0.002
H33	0.053	0.06	0.007
H34	0.059	0.063	0.004
H35	0.064	0.051	−0.013
H36	0.026	0.038	0.012
H37	0.031	0.041	0.01
H38	0.03	0.04	0.01
H39	0.031	0.04	0.009
H40	0.035	0.041	0.006
			Sum = 0.552
O41	**−0.267**	**−0.503**	**−0.236**
H42	0.267	0.235	−0.032
O43	**−0.267**	**−0.519**	**−0.252**
H44	0.267	0.236	−0.031
			Sum = −0.551

Table 7. Mulliken Charges of O_3 and Ar−CH_2−CH═CH−$(CH_2)_3$−Ar before and after Adsorption

Atoms	Before adsorption	After adsorption	Δ charges
C1	−0.044	−0.042	0.002
C2	−0.033	−0.029	0.004
C3	−0.046	−0.047	−0.001
C4	0.052	0.062	0.01
C5	−0.047	−0.061	−0.014
C6	−0.032	−0.03	0.002
C7	−0.134	−0.13	0.004
C8	**-0.015**	**0.107**	**0.122**
C9	**-0.016**	**0.097**	**0.113**
C10	−0.105	−0.097	0.008
C11	−0.069	−0.078	−0.009
C12	−0.126	−0.132	−0.006
C13	0.059	0.074	0.015
C14	−0.048	−0.052	−0.004
C15	−0.032	−0.031	0.001
C16	−0.045	−0.043	0.002
C17	−0.031	−0.031	0
C18	−0.05	−0.048	0.002
H19	0.031	0.035	0.004
H20	0.032	0.035	0.003
H21	0.033	0.029	−0.004
H22	0.027	0.044	0.017
H23	0.032	0.037	0.005
H24	0.058	0.054	−0.004
H25	0.022	0.109	0.087
H26	0.02	0.085	0.065
H27	0.041	0.067	0.026
H28	0.056	0.082	0.026
H29	0.047	0.066	0.019
H30	0.055	0.044	−0.011
H31	0.052	0.099	0.047
H32	0.049	0.051	0.002
H33	0.028	0.047	0.019
H34	0.032	0.024	−0.008
H35	0.031	0.03	−0.001
H36	0.032	0.03	−0.002
H37	0.029	0.032	0.003
H38	0.056	0.031	−0.025
			Sum = 0.519
O39	**−0.118**	**−0.276**	**−0.158**
O40	**0.236**	**0.026**	**−0.21**
O41	**−0.118**	**−0.267**	**−0.149**
			Sum = −0.517

levels are formed at −16.5 eV and E_F, which enhances the reaction activity of the H atom. Finally, after the adsorption of OH•, the 2 s orbital of O41 and the 1 s orbital of H29 have a strong localized interaction at −16.5 eV, while the 2p orbital of O41 and the 1 s orbital of H29 have a weak interaction in the range of −4.6 eV to 1.2 eV. The density of states of O43 and H27 in Figure 14b is similar to Figure 14a, and the difference is that after adsorption, the H1 s orbital generates a new energy level at −17.18 eV, and the density of states of this energy level is greater than that at −16.5 eV in Figure 14a, indicating that the interaction between O43 and H27 is more localized. In Figure 14c, after adsorption, the s and p orbitals of O39 and C8 move to the low energy level, so the energy of the adsorption configuration decreases. The 2 s and 2p orbitals of O both move from −25.7 to −24.8 eV, and the 2 s and 2p orbitals of the polarized metal complex both generate new energy levels at −24.8 eV. As a result, the above four orbitals have a strong localization effect at this energy level. The energy at −18.9 eV is mainly composed of O 2s, O 2p, and C 2p orbitals, and O 2p and C 2p orbitals interact to varying degrees in the energy range of −16.8 eV to 0.4 eV. The density of states distribution of O41 and C9 shown in Figure 14d is similar to that in Figure 14c, except that the individual peak intensities are different.

3.4. FTIR Analysis of Coal and Coal-Based Carbon Quantum Dots. Through many DFT calculations, we found that OH• and O_3 do not react with −COO and −C═O. To

https://doi.org/10.1021/acsomega.3c06525
ACS Omega 2024, 9, 753−770

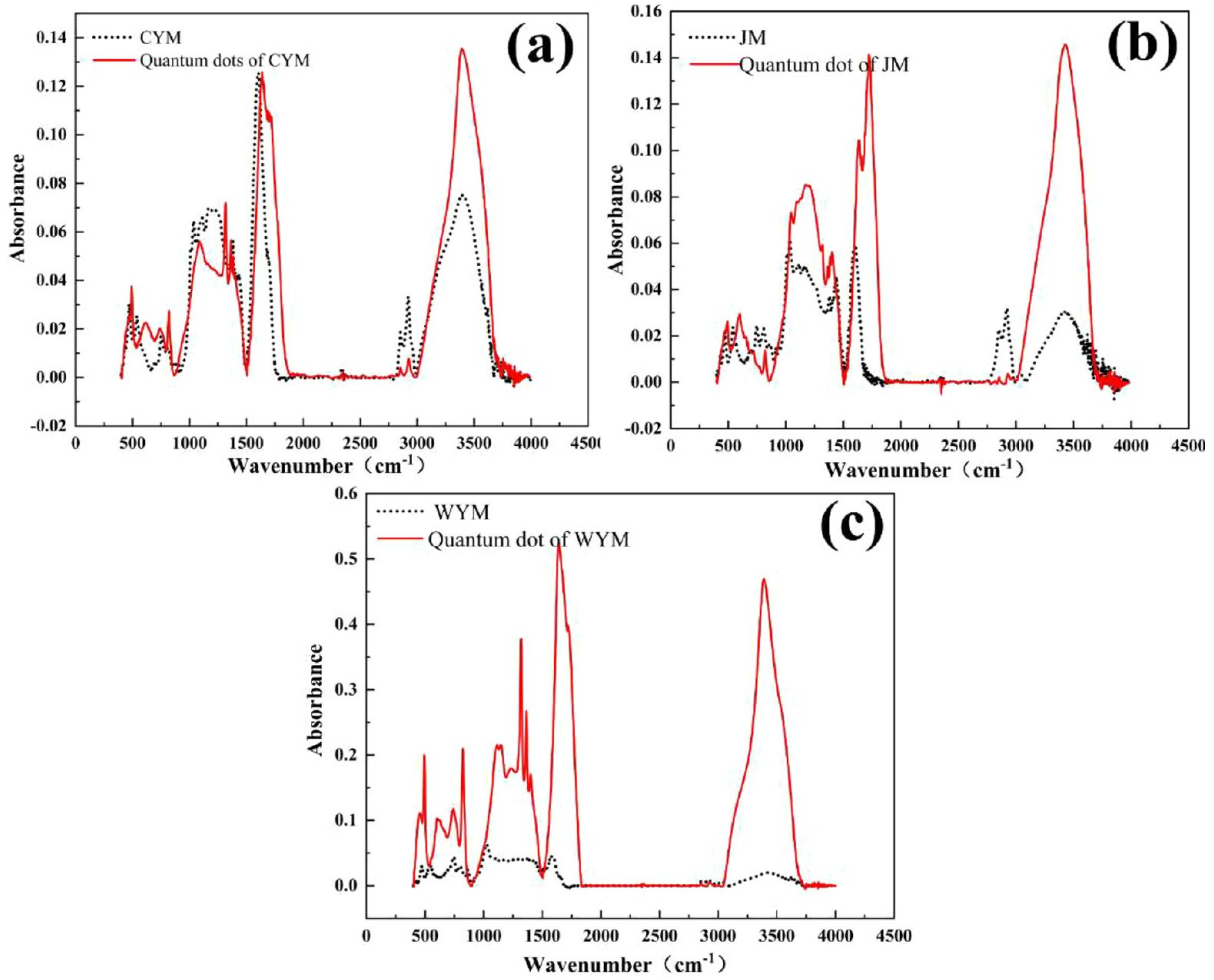

Figure 16. Infrared spectra of coal and carbon quantum dots: (a) subbituminous coal and subbituminous coal based carbon quantum dots, (b) bituminous coal and bituminous coal based carbon quantum dots, (c) anthracite and anthracite based carbon quantum dots.

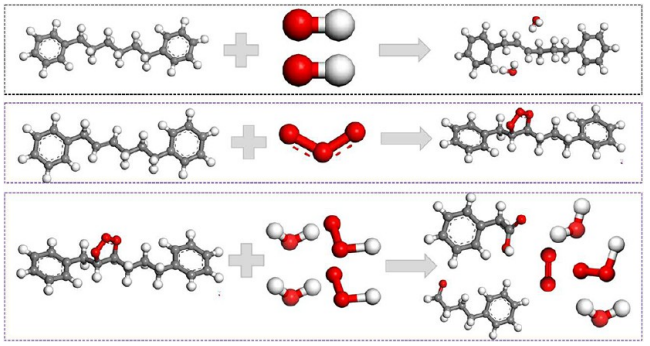

Figure 17. Main reaction process of preparing coal based carbon quantum dots by ozone oxidation of coal.

make the article more concise, the reaction process of OH• with C−OH and C−O−C is put in the supplementary document. To verify the reliability of the simulation results, the infrared spectra of the three coals and their carbon quantum dots were tested, as shown in Figure 16. After oxidation by ozone, the peak intensity of the three coal-based carbon quantum dots in the wavenumber range 3000−3570 cm^{-1} increases significantly. This is mainly due to the stretching vibration of −OH, so there is a large number of −OH in coal-based carbon quantum dots.

The increase range increases with the coal rank because with the increase in coal rank, the content of aromatic carbon increases, and then a large number of phenolic hydroxyl groups are formed by the reaction of benzene and OH• in coal. The absorption peaks near 2920 and 2850 cm^{-1} are the symmetrical and asymmetric stretching vibration absorption peaks of CH_2, respectively. In Figure 16a and b, the intensity of these two absorption peaks decreases sharply after oxidation, indicating that the methylene chain in coal is interrupted and disappears due to a large amount of oxidation. The carbon quantum dots have only a small amount of unbroken methylene chains. However, there are few methylene chains in anthracite, so the absorption peaks corresponding to 2920 and 2850 cm^{-1} in Figure 16c only decrease slightly. The wavenumber 1600−1635 cm^{-1} is the stretching vibration absorption peak of aromatic C═C, and 1696 and 1702 cm^{-1} are the stretching vibrations of carbonyl (−C═O). In Figure 16a, the strength of the C═C absorption peak before and after oxidation is basically unchanged, while the stretching vibration absorption peak of the shoulder peak −C═O is significantly enhanced; therefore, the carbon quantum dots generated by the oxidation of sub-bituminous coal contain a large number of carbonyl functional groups. In Figure 16b and c, although the intensity of the aromatic C═C absorption peak of carbon quantum dots increases, the absorption peaks of other parts increase in almost equal proportions, so the aromaticity will

https://doi.org/10.1021/acsomega.3c06525
ACS Omega 2024, 9, 753−770

not change much before and after oxidation. Similar to Figure 16a, the stretching vibration peak of carbonyl (−C═O) on the shoulder of bituminous coal (Figure 16b) is significantly enhanced and the proportion increases. Therefore, carbon quantum dots contain more carbonyl groups than coal. The increase in phenolic hydroxyl content leads to the enhancement of the C−O stretching vibration absorption peak in phenolic hydroxyl groups in the wavenumber range 1100−1300 cm^{-1}. In conclusion, the calculated results in this paper are in good agreement with the FTIR test.

In summary, the main reaction process of ozone oxidation of coal to prepare coal based carbon quantum dots is shown in Figure 17. From the figure, it can be seen that the methylene chains in coal are oxidized by hydroxyl radicals and ozone and then break in an aqueous solution of ozone, resulting in the separation of the basic structural units of coal from each other.

4. CONCLUSIONS

In this paper, we studied the oxidation behavior of ozone on the surface of coal through experiments and DFT methods and separated the oxides of the coal molecular fragments (coal-based carbon quantum dots). Characterized by transmission electron microscopy, the morphology, size distribution, and lattice fringes of coal-based carbon quantum dots were obtained. From the perspective of visualization, the molecular structure characteristics of sub-bituminous coal, bituminous coal, and anthracite are explored. It is found that there are large-scale regular structures and amorphous components in all three coals.

The electronic properties of five simplified coal molecules (Ar−$(CH_2)_6$−Ar, Ar−$(CH_2)_2$−CHOH−$(CH_2)_3$−Ar, Ar−$(CH_2)_2$−O− (CH2)$_3$−Ar, A-$(CH_2)_2$−COO−$(CH_2)_2$−Ar, and Ar−$(CH_2)_2$−C═O−$(CH_2)_3$−Ar) were studied. OH• and O_3 with different functional groups were studied from the perspective of frontier orbital theory, electrostatic potential, and Fukui function, and the active sites of each molecule were clarified. When different oxygen-containing functional groups were introduced, the frontier orbitals of the molecules changed significantly, indicating that the oxygen-containing functional groups have a significant impact on the properties of coal. Except for the frontier orbital coefficient of the oxygen atom in − OH being 0.01, the frontier orbital coefficient of the oxygen atom in the other functional groups is 0.1−0.6, which is the active site of the coal molecule. The Fukui function results show that the H atom in the methylene and the oxygen atom in the oxygen-containing functional groups of the five coal molecules contain a large f^- index; therefore, they are vulnerable to electrophilic attacks and lose electrons. The microscopic adsorption mechanism of OH• and O_3 on Ar−$(CH_2)_6$−Ar and Ar−CH_2−CH═CH−$(CH_2)_3$−Ar was clarified from the aspects of the reaction process, energy change, Mulliken charge population, total charge density, deformation charge density, and density of states.

By analyzing the infrared spectra of coal and corresponding carbon quantum dots, it was found that the content of functional groups such as −C═O and −OH in the carbon quantum dots generated by coal oxidation increased significantly, while the content of CH_2 decreased sharply. This phenomenon is consistent with the simulation results presented in this paper.

■ ASSOCIATED CONTENT

Supporting Information

The Supporting Information is available free of charge at https://pubs.acs.org/doi/10.1021/acsomega.3c06525.

Oxidation reaction process of bituminous and anthracite by ozone, the process of oxidation of oxygen-containing functional groups by hydroxyl radicals, morphology of coal based carbon quantum dots of bituminous coal and anthracite (PDF)

■ AUTHOR INFORMATION

Corresponding Authors

Wenli Liu − *School of Chemical and Environment Engineering, China University of Mining & Technology (Beijing), Beijing 100083, China*; Phone: +86 13910724272; Email: liuwenli08@163.com

Qiming Zhuo − *School of Chemical and Environment Engineering, China University of Mining & Technology (Beijing), Beijing 100083, China*; orcid.org/0000-0001-7029-7549; Phone: +86 15201312943; Email: zhuoqiming92@126.com

Author

Qing Luo − *School of Materials and Chemical Engineering, Henan University of Urban Construction, Pingdingshan 467036 Henan Province, China; School of Chemical and Environment Engineering, China University of Mining & Technology (Beijing), Beijing 100083, China*; orcid.org/0000-0001-9226-5759

Complete contact information is available at: https://pubs.acs.org/10.1021/acsomega.3c06525

Author Contributions

The manuscript was completed through the contributions of all authors. **Qing Luo:** Writing-Original draft preparation, Software, Data curation, Formal analysis, Visualization. **Wenli Liu:** conceptualization methodology, funding acquisition. **Qiming Zhuo:** Data curation, Supervision, Funding acquisition.

Notes

The authors declare no competing financial interest.

■ ACKNOWLEDGMENTS

This research was funded by the National Natural Science Foundation of China (No. 51974324 and No. 52104281) and the Open Foundation of State Key Laboratory of Mineral Processing (No. BGRIMM-KJSKL-2020-22).

■ REFERENCES

(1) Chang, Z.; Chen, X.; Peng, Y. Understanding and improving the flotation of coals with different degrees of surface oxidation. *Powder Technol.* **2017**, *321*, 190−6.

(2) Zhang, Y.; Zhang, K.; Jia, K.; Liu, G.; Ren, S.; Li, K.; et al. Preparation of coal-based graphene quantum dots/α-Fe_2O_3 nanocomposites and their lithium-ion storage properties. *Fuel* **2019**, *241*, 646−52.

(3) Wang, Y.; Hu, A. Carbon quantum dots: synthesis, properties and applications. *Journal of Materials Chemistry, C materials for optical and electronic devices* **2014**, *2*, 6921.

(4) Xu, Y.; Wang, S.; Hou, X.; Sun, Z.; Jiang, Y.; Dong, Z.; et al. Coal-derived nitrogen, phosphorus and sulfur co-doped graphene quantum dots: A promising ion fluorescent probe. *Appl. Surf. Sci.* **2018**, *445*, 519−26.

(5) Dong, Y.; Lin, J.; Chen, Y.; Fu, F.; Chi, Y.; Chen, G. Graphene quantum dots, graphene oxide, carbon quantum dots and graphite nanocrystals in coals. *Nanoscale* **2014**, *6*, 7410.
(6) Liu, X.; Song, D.; He, X.; Nie, B.; Wang, L. Insight into the macromolecular structural differences between hard coal and deformed soft coal. *Fuel* **2019**, *245*, 188−97.
(7) Liu, X.; Song, D.; He, X.; Nie, B.; Wang, Q.; Sun, R.; et al. Coal macromolecular structural characteristic and its influence on coalbed methane adsorption. *Fuel* **2018**, *222*, 687−94.
(8) Tang, L.; Chen, S.; Gui, D.; Zhu, X.; He, H.; Tao, X. Effect of removal organic sulfur from coal macromolecular on the properties of high organic sulfur coal. *Fuel* **2020**, *259*, 116264.
(9) Zhang, H.; Xi, P.; Zhuo, Q.; Liu, W. Construction of Molecular Model and Adsorption of Collectors on Bulianta Coal. *Molecules* **2020**, *25* (17), 4030.
(10) Liu, J.; Jiang, Y.; Yao, W.; Jiang, X.; Jiang, X. Molecular characterization of Henan anthracite coal. *Energy Fuels* **2019**, *33* (7), 6215−25.
(11) Wang, J.-P.; Li, G.-Y.; Guo, R.; Li, A.-Q.; Liang, Y.-H. Theoretical and experimental insight into coal structure: establishing a chemical model for Yuzhou lignite. *Energy Fuels* **2017**, *31* (1), 124−32.
(12) Wang, J.; He, Y.; Li, H.; Yu, J.; Xie, W.; Wei, H. The molecular structure of Inner Mongolia lignite utilizing XRD, solid state 13C NMR, HRTEM and XPS techniques. *Fuel* **2017**, *203*, 764−73.
(13) Xie, K.-C.. *Structure and Reactivity of Coal*; Springer: Berlin, 2015.
(14) Peng, H.; Travas-Sejdic, J. Simple Aqueous Solution Route to Luminescent Carbogenic Dots from Carbohydrates. *Chem. Mater.* **2009**, *21* (23), 5563.
(15) Li, M.; Hu, C.; Yu, C.; Wang, S.; Zhang, P.; Qiu, J. Organic amine-grafted carbon quantum dots with tailored surface and enhanced photoluminescence properties. *Carbon* **2015**, *91*, 291−7.
(16) Zhang, Z.; Chen, Y. A constrained intrinsic cohesive finite element method with little stiffness reduction for fracture simulation. *Engineering Fracture Mechanics* **2015**, *136*, 213−25.
(17) Liu, X.; Hao, J.; Liu, J.; Tao, H. Green synthesis of carbon quantum dots from lignite coal and the application in $Fe3^{+}$ detection. *Iop Conference* **2018**, *113*, No. 012063.
(18) Das, R.; Bandyopadhyay, R.; Pramanik, P. Carbon quantum dots from natural resource: A review. *Materials today chemistry* **2018**, *8*, 96−109.
(19) Mintz, K. J.; Zhou, Y.; Leblanc, R. M. Recent development of carbon quantum dots regarding their optical properties, photoluminescence mechanism, and core structure. *Nanoscale* **2019**, *11* (11), 4634−52.
(20) Wang, X.; Yang, P.; Feng, Q.; Meng, T.; Wei, J.; Xu, C.; et al. Green preparation of fluorescent carbon quantum dots from cyanobacteria for biological imaging. *Polymers* **2019**, *11* (4), 616.
(21) Limosani, F.; Bauer, E. M.; Cecchetti, D.; Biagioni, S.; Orlando, V.; Pizzoferrato, R.; et al. Top-down N-doped carbon quantum dots for multiple purposes: Heavy metal detection and intracellular fluorescence. *Nanomaterials* **2021**, *11* (9), 2249.
(22) Murugan, N.; Prakash, M.; Jayakumar, M.; Sundaramurthy, A.; Sundramoorthy, A. K. Green synthesis of fluorescent carbon quantum dots from Eleusine coracana and their application as a fluorescence 'turn-off'sensor probe for selective detection of Cu^{2+}. *Appl. Surf. Sci.* **2019**, *476*, 468−80.
(23) Wu, P.; Li, W.; Wu, Q.; Liu, Y.; Liu, S. Hydrothermal synthesis of nitrogen-doped carbon quantum dots from microcrystalline cellulose for the detection of Fe^{3+} ions in an acidic environment. *RSC Adv.* **2017**, *7* (70), 44144−53.
(24) Arumugam, N.; Kim, J. Synthesis of carbon quantum dots from Broccoli and their ability to detect silver ions. *Mater. Lett.* **2018**, *219*, 37−40.
(25) Li, X.; Ma, S.; Qian, H.; Zhang, Y.; Zuo, S.; Yao, C. Upconversion nanocomposite CeO2:Tm3+/attapulgite intermediated by carbon quantum dots for photocatalytic desulfurization. *Powder Technol.* **2019**, *351*, 38−45.
(26) Saikia, M.; Das, T.; Dihingia, N.; Fan, X.; Silva, L. F. O.; Saikia, B. K. Formation of carbon quantum dots and graphene nanosheets from different abundant carbonaceous materials. *Diamond Relat. Mater.* **2020**, *106*, 107813.
(27) Jia, J.; Sun, Y.; Zhang, Y.; Liu, Q.; Cao, J.; Huang, G.; Xing, B.; Zhang, C.; Zhang, L.; Cao, Y.; et al. Facile and efficient fabrication of bandgap tunable carbon quantum dots derived from anthracite and their photoluminescence properties. *Frontiers in chemistry* **2020**, *8*, 123.
(28) Cai, Y.; Du, M.; Wang, S.; Liu, L. Determination of oxidation properties and flotation parameters of low-rank coal slimes. *Powder Technol.* **2019**, *353*, 20−6.
(29) Azad, T.; Schuler, J. D.; Auad, M. L.; Elder, T.; Adamczyk, A. J. Model lignin oligomer pyrolysis: Coupled conformational and thermodynamic analysis of β-O-4′ bond cleavage. *Energy Fuels* **2020**, *34* (8), 9709−24.
(30) Wang, M.; Li, P.; Jia, X.; Liu, W.; Shao, Y.; Hu, W.; et al. Efficient Strategy for the Calculation of Solvation Free Energies in Water and Chloroform at the Quantum Mechanical/Molecular Mechanical Level. *J. Chem. Inf. Model.* **2017**, *57* (10), 2476−89.
(31) Choi, C. H.; Kertesz, M. Conformational Information from Vibrational Spectra of Styrene, trans-Stilbene, and cis-Stilbene. *J. Phys. Chem. A* **1997**, *101*, 3823.
(32) Hamad, S.; Lago, S.; Mejías, J. A Computational Study of the Hydration of the OH Radical. *J. Phys. Chem. A* **2002**, *106* (39), 9104−13.
(33) Khalack, J. M.; Lyubartsev, A. P. Solvation Structure of Hydroxyl Radical by CarParrinello Molecular Dynamics. *J. Phys. Chem. A* **2005**, *109* (2), 378.
(34) Li, Y.; Shang, H.; Zhang, Q.; Elabyouki, M.; Zhang, W. Theoretical study of the structure and properties of Ni/V porphyrins under microwave electric field: A DFT study. *Fuel* **2020**, *278*, 118305.
(35) de la Torre, B.; Matej, A.; Sanchez-Grande, A.; Cirera, B.; Mallada, B.; Rodriguez-Sanchez, E.; Santos, J.; Mendieta-Moreno, J. I.; Edalatmanesh, S.; Lauwaet, K. Tailoring π-conjugation and vibrational modes to steer on-surface synthesis of pentalene-bridged ladder polymers. *Nat. Commun.* **2020**, *11*, 4567.
(36) Vassilev, P.; Louwerse, M.; Baerends, E. Ab initio molecular dynamics simulation of the OH radical in liquid water. *Chemical Physics Letters - CHEM PHYS LETT* **2004**, *398*, 212−6.
(37) Xu, S.; Wang, G.; Liu, H. M.; Wang, L. J.; Wang, H. F. A DMol 3 study on the reaction between trans-resveratrol and hydroperoxyl radical: Dissimilarity of antioxidant activity among O−H groups of trans-resveratrol. *Journal of Molecular Structure Theochem* **2007**, *809* (1), 79−85.
(38) Karadakov, P. B.; Saito, S. Can Anti-Aufbau DFT Calculations Estimate Singlet Excited State Aromaticity? Correspondence on "Dibenzoarsepins: Planarization of 8π-Electron System in the Lowest Singlet Excited State. *Angew. Chem., Int. Ed.* **2020**, *59* (24), 9228−30.
(39) Hohenberg, P.; Kohn, W. Inhomogeneous electron gas. *Physical review* **1964**, *136* (3B), B864.
(40) Basiuk, V. A. Electron smearing in DFT calculations: A case study of doxorubicin interaction with single-walled carbon nanotubes. *Int. J. Quantum Chem.* **2011**, *111* (15), 4197−205.
(41) Berry, R. S. Time-Dependent Measurements and Molecular Structure: Ozone. *Rev. Mod. Phys.* **1960**, *32* (2), 447−54.
(42) Huber, K. P.; Herzberg, G. *Molecular Spectra and Molecular Structure: IV Constants of Diatomic Molecules*; Springer, 1979.
(43) Jiang, J.; Yang, W.; Cheng, Y.; Liu, Z.; Zhang, Q.; Zhao, K. Molecular structure characterization of middle-high rank coal via XRD, Raman and FTIR spectroscopy: Implications for coalification. *Fuel* **2019**, *239*, 559−72.
(44) Dun, W.; Guijian, L.; Ruoyu, S.; Xiang, F. Investigation of Structural Characteristics of Thermally Metamorphosed Coal by FTIR Spectroscopy and X-ray Diffraction. *Energy Fuels* **2013**, *27*, 5823−5830.
(45) Chen, J.; Min, F-f; Liu, L-y The interactions between fine particles of coal and kaolinite in aqueous, insights from experiments and molecular simulations. *Appl. Surf. Sci.* **2019**, *467−468*, 12−21.

https://doi.org/10.1021/acsomega.3c06525
ACS Omega 2024, 9, 753−770

(46) Li, B.; Liu, S.; Guo, J.; Zhang, L. Interaction between low rank coal and kaolinite particles: A DFT simulation. *Appl. Surf. Sci.* **2018**, *456*, 215−20.
(47) Mizuno, T.; Tsuno, H.; Yamada, H. Development of ozone self-decomposition model for engineering design. *Ozone: Science and Engineering* **2007**, *29* (1), 55−63.
(48) Ershov, B. G.; Morozov, P. A. The kinetics of ozone decomposition in water, the influence of pH and temperature. *Russian Journal of Physical Chemistry A* **2009**, *83* (8), 1295−9.
(49) Hirahara, Y.; Iwata, K.; Nakamuro, K. Effect of Citric Acid on Prolonging the Half-life of Dissolved Ozone in Water. *Food Safety* **2019**, *7* (4), 90−4.
(50) Gardoni, D.; Vailati, A.; Canziani, R. Decay of Ozone in Water: A Review. *Ozone: Science & Engineering: The Journal of the International Ozone Association* **2012**, *34*, 233.
(51) Westerhoff, P.; Song, R.; Amy, G.; Minear, R. Applications of Ozone Decomposition Models. *Ozone: Sci. Eng.* **1997**, *19*, 55−73.
(52) Xiang, Q.; Yu, J.; Wong, P. K. Quantitative characterization of hydroxyl radicals produced by various photocatalysts. *J. Colloid Interface Sci.* **2011**, *357* (1), 163−7.
(53) Wang, J. L.; Xu, L. J. Advanced oxidation processes for wastewater treatment: formation of hydroxyl radical and application. *Critical reviews in environmental science and technology* **2012**, *42* (3), 251−325.
(54) Zhang, X, Zhang, J. *Coal Chemical*; China University of Mining and Technology Press, 2012.
(55) Corrie, A. M.; Williams, D. R. Thermodynamic considerations in co-ordination. Part XXIV. Gibbs free-energy changes, enthalpies, and entropies of formation of complexes of glycinate, glycylglycinate, glycylglycylglycinate, cysteinate, and glutathionate with hydrogen and lead (II) ions and suggested aqueous structures. *J. Chem. Soc., Dalton Trans.* **1976**, *12*, 1068−72.
(56) Bao, L.; Zhang, Z. L.; Tian, Z. Q.; Zhang, L.; Liu, C.; Lin, Y.; et al. Electrochemical Tuning of Luminescent Carbon Nanodots: From Preparation to Luminescence Mechanism. *Adv. Mater.* **2011**, *23* (48), 5801−6.
(57) Hu, C.; Yu, C.; Li, M.; Wang, X.; Yang, J.; Zhao, Z.; et al. Chemically Tailoring Coal to Fluorescent Carbon Dots with Tuned Size and Their Capacity for Cu(II) Detection. *Small* **2014**, *10* (23), 4926−33.
(58) Saikia, M.; Hower, J. C.; Das, T.; Dutta, T.; Saikia, B. K. Feasibility study of preparation of carbon quantum dots from Pennsylvania anthracite and Kentucky bituminous coals. *Fuel* **2019**, *243*, 433−40.
(59) Singamaneni, S. R.; van Tol, J.; Ye, R.; Tour, J. M. Intrinsic and extrinsic defects in a family of coal-derived graphene quantum dots. *Appl. Phys. Lett.* **2015**, *107* (21), 4015.
(60) Qin, Z. New advances in coal structure model. *International Journal of Mining Science and Technology* **2018**, *28* (4), 541−59.
(61) Zhang, H.; Xi, P.; Zhuo, Q.; Liu, W. Construction of Molecular Model and Adsorption of Collectors on Bulianta Coal. *Molecules* **2020**, *25* (17), 4030.
(62) Fukui, K. Role of frontier orbitals in chemical reactions. *science* **1982**, *218* (4574), 747−54.
(63) Yang, W.; Parr, R. G. Hardness, softness, and the fukui function in the electronic theory of metals and catalysis. *Proc. Natl. Acad. Sci. U. S. A.* **1985**, *82* (20), 6723−6.
(64) Dewar, M. J. A critique of frontier orbital theory. *Journal of Molecular Structure: THEOCHEM* **1989**, *200*, 301−23.
(65) Politzer, P.; Laurence, P. R.; Jayasuriya, K. Molecular electrostatic potentials: an effective tool for the elucidation of biochemical phenomena. *Environ. Health Perspect.* **1985**, *61*, 191−202.

https://doi.org/10.1021/acsomega.3c06525
ACS Omega 2024, 9, 753−770